공학박사 학위논문

Stretchable Electrode Using Silver Nanowires and Elastomeric Block-Copolymer Nanocomposite for Biomedical Devices

은나노와이어/탄성 블록-공중합체의 나노

복합체를 이용한 신축성전극과 의료소자로의 활용

2017년 8월

서울대학교 대학원

화학생물공학부

최 수 지

Stretchable Electrode Using Silver Nanowires and Elastomeric Block-Copolymer Nanocomposite for Biomedical Devices

지도 교수 김 대 형

이 논문을 공학박사 학위논문으로 제출함
2017년 07월

서울대학교 대학원
화학생물공학부
최 수 지

최수지의 공학박사 학위논문을 인준함
2017년 07월

위 원 장 _____ (인)

부위원장 _____ (인)

위 원 _____ (인)

위 원 _____ (인)

위 원 _____ (인)

Abstract

Stretchable Electrode Using Silver Nanowires and Elastomeric Block-Copolymer Nanocomposite for Biomedical Devices

Suji Choi
School of Chemical and Biological Engineering
The Graduate School
Seoul National University

Stretchable conductors with high conductivity and stable performance under deformation are potentially highly useful for fabricating improved stretchable and wearable devices. Stretchable conductive nanocomposites comprising a percolation network of various conductive nanomaterials are being vigorously investigated to utilize their outstanding electrical and mechanical properties. Silver nanowire-based stretchable conductor, in particular, showed stable electrical performance under extreme mechanical

deformation because of its intrinsically high conductivity and high aspect ratio. This dissertation describes the synthesis of highly conductive and stretchable silver nanowire/elastomer nanocomposite and device fabrication processing to minimize strain, so as to develop stretchable bio-medical devices such as articular thermotherapy device and epicardial mesh for cardiac resynchronizing therapy.

First, a soft, thin, and stretchable heater was developed by using a nanocomposite of silver nanowires and a poly(styrene-butadiene-styrene) (SBS) elastomer. A highly conductive and homogeneous nanocomposite was formed by the ligand exchange reaction of silver nanowires. By patterning the nanocomposite with serpentine-mesh structures, conformal lamination of devices on curvilinear joints was achieved, which led to effective heat transfer even during motion. The combination of a homogeneous conductive elastomer, a stretchable design, and a custom-designed electronic band helped create a novel wearable heater system that can be used for long-term and continuous articular thermotherapy.

Second, the epicardial device was developed to improve the systolic function in a diseased rat heart without impeding the diastolic function by wrapping the device around the rat heart. The epicardial mesh was designed with elastic properties that are nearly identical to those of the epicardial tissue of the rat heart, and hence, the mesh functioned as a structural component by reducing the host-myocardial wall stress. In addition, the

epicardial mesh was able to detect electrical signals reliably on the moving rat heart as well as activate the entire ventricular myocardium simultaneously through synchronized electrical stimulation over the ventricles. Electrically and mechanically optimized epicardial mesh using the ligand-exchanged silver nanowire and SBS nanocomposite improved the hemodynamics in experimental heart failure in the rodent.

Finally, a new biocompatible and conductive nanocomposite was developed for stretchable bio-medical devices. As the stretchable conductive composites become widely available as an implantable biomedical device, its biocompatibility must be improved. To overcome the limited biocompatibility of the silver-based nanocomposite, a gold nanoshell was encapsulated on the ultra-long silver nanowire (Ag@AuNW) to prevent the toxic silver ion from leaching out. The formed novel percolation network in the fabricated Ag@AuNW and SBS composite showed stable electrical performance of stretchable conductors under extreme mechanical strain (up to 180%), resulting in high conductivity and stretchabiltiy. A 3D customized cardiac mesh-sock for the porcine heart was fabricated using the Ag@AuNW/SBS composite. In an acute-MI porcine heart, the progress of heart disease was monitored by chronological cardiac activity mapping through a customized 3D mesh sock. Multi-channel electrodes on the epicardial surface diversified the pacing sites on the dysfunctional heart, enabling disease-specific treatment by offering various electrical treatment

options without any spatial limitation.

Keyword : stretchable conductor, silver nanowire-elastomer composite, wearable medical device, implantable device, stretchable thermotherapy, cardiac mesh

Student Number : 2012-20982

Table of Contents

Chapter 1. Strategy of fabrication for stretchable conductor and applications in stretchable electronics..... 1

1.1. Introduction 1

1.2. Nanomaterials, assembly, and device designs for flexible and stretchable electronics..... 4

1.3 strategy for stretchable conductor to enhance stretchability 7

1.4. Applications of stretchable conductor using carbon based material and silver based materials..... 12

1.5 Reference..... 22

Chapter 2. Stretchable Heater Using Ligand-Exchanged Silver Nanowire Nanocomposite for Wearable Articular Thermotherapy..... 26

2.1 Introduction 26

2.2 Experimental Section..... 28

2.3 Result and Discussion..... 36

2.4 Conclusion..... 57

2.5 Reference 58

Chapter 3. Electromechanical cardioplasty using a wrapped soft, highly conductive epicardial mesh. 63

3.1 Introduction 63

3.2 Experimental Section 66

3.3 Result and Discussion 68

3.4 Conclusion 91

3.5 Reference 92

Chapter 4. Highly conductive and biocompatible stretchable conductor for 3D multi-polar cardiac sock 95

4.1 Introduction 95

4.2 Experimental Section 97

4.3 Result and Discussion 101

4.4 Conclusion 121

4.5 Reference 122

Bibliography 124

Abstract in Korean 128

List of Figure

Figure 1.1 Nanomaterials, assembly, and device designs for flexible and stretchable electronics..... 6

Figure 1.2 Strategy for stretchable conductor to enhance stretchability. 10

Figure 1.3 Skin-laminated piezoresistive strain sensors. 14

Figure 1.4 Implantable bioelectronics based on carbon nanotubes. 16

Figure 1.5 Stretchable electrode and energy devices using silver based stretchable conductor. 20

Figure 2.1 Ligand exchange of silver nanowire (LE-AgNW) and LE-AgNW/SBS composite. 43

Figure 2.2 The contour maps of nanocomposites before and after ligand exchange Ag NW. 44

Figure 2.3 PDMS mold fabrication and its effects..... 45

Figure 2.4 Fabrication of mesh heater and heater performance..... 46

Figure 2.5 Serpentine mesh design effect. 47

Figure 2.6 Charaterizations of mesh heater..... 48

Figure 2.7 Mechanical and electrical characterization of mesh heater. . 49

Figure 2.8 Strain anaysis from various joints. 50

Figure 2.9 Application for thermotherapy..... 51

Figure 2.10 Irritation test. 52

Figure 2.11 Integration of customized electronic band. 53

Figure 2.12 Computer simulation of heat diffusion. 54

Figure 2.13 Computer simulation model and heat diffusion under stretching. 55

Figure 2.14 The physiologic effect of thermotherapy. 56

Figure 3.1 Strategy of materials and design for epicardial mesh. 71

Figure 3.2 Fabrication of elastic epicardial mesh. 73

Figure 3.3 Computer simulation for effects of epicardial mesh. 75

Figure 3.4 Coupling effect of the epicardial mesh to the rat heart. 78

Figure 3.5 Hemodynamic and structural effects of electromechanical cardioplasty. 79

Figure 3.6 Comparision of QRS duration. 82

Figure 3.7 The relation of heart rates to QRS durations, and epicardial mesh pacing at 90% of the baseline cycle lengths. 83

Figure 3.8 The effect of electrical stimulation on cardiac electrical and mechanical function. 84

Figure 3.9 Echocardiographic data LVEDD, LVESD, and FS in control and 8-week post-MI rats. 85

Figure 3.10 Speckle tracking radial strain data in control and 8-week post-

MI hearts. 86

Figure 3.11 LV contractility index, dP/dtmax, during right atrial pacing (RAP) and MeshP in controls and 8-week post-MI rats. 87

Figure 3.12 Histological analysis for biocompatibility test of epicardial mesh. 89

Figure 3.13 Biocompatibility of the gold coated device. 90

Figure 4.1 Biocompatible gold shell silver nanowire (Ag@Au NW) and SBS nanocomposite. 106

Figure 4.2 SEM images of Ag@Au/SBS composites depending on the fabrication temperature. 107

Figure 4.3 Mechanical and electrical performance of the Ag@Au/SBS composite. 108

Figure 4.4 Electrochmical properties of Ag@Au/SBS electrode. 111

Figure 4.5 Fabrication of 3D cardiac sock-mesh and electrical and mechanical properties. 114

Figure 4.6 Recording intracardia electrogram form 3D cardiac sock-mesh *in vivo.* 118

Figure 4.7 Mapping based on simultaneouly recorded signals and hemodynamic response from streotactic pacing. 119

Figure 4.8 Recorded intracardiac electrograms from multi-polar 3D cardiac

mesh-sock electrodes after one hour LAD ligation. 1 2 0

Chapter 1. Strategy of fabrication for stretchable conductor and applications in stretchable electronics

1.1. Introduction

Over a decade, there are many interdisciplinary efforts for flexible and stretchable electronic system/devices, which encourages the revolutionizing development of bioelectronics devices in terms of materials, designs, and systems. These developments lead people to monitor emanating signals conveniently from human body through electrophysiological sensors(i.e. electrocardiogram (ECG), electromyogram (EMG)), mechanical sensors with electronics skin (i.e., strain, pressure), and provide the appropriate treatments by therapeutic devices (i.e., electrical stimulation therapy, drug delivery system). The soft bio-electronic systems composed of various electronic components such as electrodes, integrated circuits, sensors and actuators. Since the bioelectronic devices should be compatible with soft and movable human tissue and body, the each electronic components also require not only mechanical robustness and softness, but also strain tolerance with high performance stability. However, the most of established materials such as metals, inorganic thin film, that are conventionally used for these electrical components are intrinsically stiff and brittle although they have high electrical quality and good uniformity.

In order to enhance soft, flexible, and stretchable bio-electronics system, there are three representative strategies to overcome the limitation of intrinsic materials. First, non-stretchable materials can be patterned with buckled or serpentine structure that can endure applied strain on the electronic system, showing high performance of intrinsic materials. Second, organic materials are utilized as active components and conductors of bioelectronics. The organic bio-electronics have high flexibility, low-cost processability, but its performance is not good as much as bulk inorganic materials properties. Third, flexible and stretchable electronics system that utilized synthesized nanomaterials that have their unique properties due to its nano-sized dimension. Especially, stretchable conductor is one of the most important electrical components in stretchable electronics. 1D structural conductive nanomaterials such as carbon nanotube and metal nanowire are attractive as a conductive fillers in elastomer, which can make efficient electrical percolation materials in the polymeric media, thus the electrical conduction can maintain under mechanical strains. Silver nanowire among the various metal nanowires, has intrinsically high conductivity, 1D structure, and easy- producibility gives many benefits to fabricate high performance of stretchable conductors. Integration with these stretchable conductors and device design process such as buckling, serpentine structure, kirigami and knitted expand the application beyond what many thin film conductive materials have.

The dissertation herein provide a brief introduction of nanostructured materials, related engineering technologies with emphasis on device application using the conductive stretchable nanocomposite. The high conductive and stretchable mesh patterned electrodes made of silver nanowires/rubber nanocomposite shows various applications as wearable and implantable biomedical devices.

1.2. Nanomaterials, assembly, and device designs for flexible and stretchable electronics

Figure 1.1a shows representative forms of nanomaterials (0D, 1D, and 2D) for flexible and stretchable devices. The nanoscale dimensions of the materials dramatically decrease flexural rigidity of devices while acting as electrodes, transport channels, and light-emitting/photon-absorption materials. Zero dimensional nanoparticles (NPs; left top) have unique properties due to quantum confinement and large surface area.[1,2] One dimensional carrier transport is more efficient in nanowires (NWs; right top)[3] and carbon nanotubes (CNTs; left bottom)[4] compared to transport properties in NPs. The aligned configurations and/or percolated networks form electronic devices with robust interconnections in channels and electrodes. Two dimensional NMs (right bottom)[5] show enhanced charge transport characteristics in planar device structures. The decreased rigidity owing to nanoscale dimensions helps mitigate the risks of mechanical failures under flexing/stretching cycles.

In the large area array of micro-/nano-devices, the uniformity of device performance is a key requirement. Although nanoscale materials are uniformly fabricated/synthesized, their assembled architecture can be non-uniform. Figure 1.1b shows examples for the assembly of 0D, 1D, and 2D materials. Langmuir-Blodgett (LB) technique utilizes an air-water interface

to assemble a uniform, large area monolayer of nanomaterials (left top).[6] Repeating the LB process can form double or triple monolayers. The dry contact printing is another effective method to align vertically grown NWs (right top).[7] Contacting and sliding transfer NWs onto the receiver substrate. Dispersed 1D nanomaterials in a solution, such as CNTs, can be spray-coated (left bottom),[8] creating a uniform random network of CNTs over large areas. 2D NMs are transfer printed using elastomeric stamps (right bottom).[9]

In addition to the intrinsic flexibility of nanomaterials, advanced device design strategies have been used to enhance system-level deformations, as shown in Figure 1.1c. The induced strains are linearly and inversely proportional to thickness and bending radii, respectively. Reducing device thickness, therefore, decreases induced strains at the same bending radius (left top).[10] Locating active regions between top and bottom layers of the same structures, *i.e.*, in the neutral mechanical plane (NMP) region where compressive and tensile strains are compensated, mitigates risks of mechanical fractures (right top).[11] Buckling enables not only bending but also stretching through elongation and contraction of wavy structures (left bottom).[12,13] Large stretchability is obtained via fractal/serpentine structures (right bottom).[14] These novel device structures enable new classes of wearable/implantable systems.

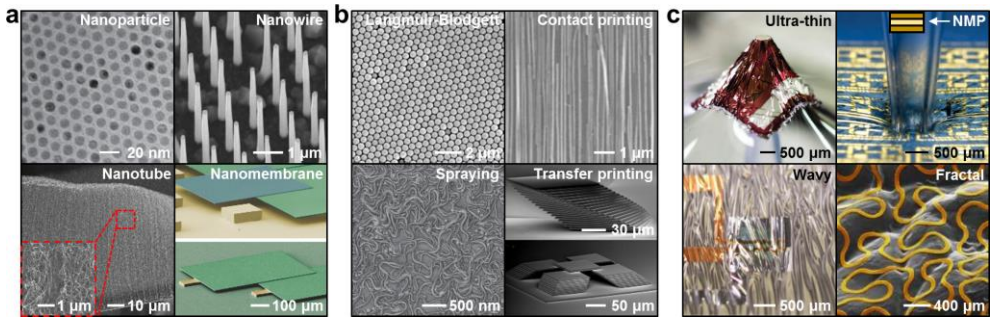

Figure 1.1 Nanomaterials, assembly, and device designs for flexible and stretchable electronics.

(a) Representative forms of nanomaterials: iron oxide nanoparticles (0D; left top), GaAs vertical NWs (1D; right top), vertical aligned carbon nanotube (CNT) (1D; left bottom), and Si NM (2D; right bottom)[1,3-5]. b) Representative assembly method for nanomaterials. Langmuir-Blodgett assembly of nanoparticles (left top), contact printing of vertical growth Si NWs (right top), spraying coating of CNT (left bottom), and Si NMs stacked by transfer printing (right bottom)[6-9]. c) Device design strategies for flexible/stretchable electronics. Ultrathin (left top), neutral mechanical plane (NMP) (right top), wavy (left bottom), and fractal (right bottom) structures enhance the system-level deformability[10-12,14]. Reproduced with permission. Copyright 2016, WILEY-VCH Verlag GmbH & Co. KGaA, Weinheim

1.3 strategy for stretchable conductor to enhance stretchability

Although intrinsic conductivity and mechanical properties of stretchable conductors are important, the fabrication process should be carefully optimized depending on chemical and physical characterizstics of the materials for the maximum performance. Although general strategy of stretchable devices that mentioned in a previous chapter can be adopted for stretchable conductor, multi-layer process or chemical additives in the stretchable conductor can also enhance the performance of the composites, which cannot be conducted by conventioanl photolithograpy process.

When the conductive filler has similar chemical property with polymer, the conductive filler can be blended with polymer matrix (Figure 1.2a). Carbon based materials has hydrophobic property which is comparable with PDMS rubber. Although once crosslinking reaction is occurred, the PDMS cannot dissolved in solvent, PDMS precursor can be dissolved in hexane and toluene before it is cured. Therefore, there are many application using blends of CNT or carbon black and PDMS as a stretchable conductor. CPDMS composed of carbon black and PDMS can be bladed on the grooved substrate for mechanical strain sensor (Figure 1.2b, left).[15] Moreover, high viscous blending solution of CNT and PDMS in hexane can be exploited with nozzle jet printing to make patterns for pressure sensor

and strain sensor (Figure 1.2b, middle).[16] As a mentioned in the previous chapter, Ag NW which has high intrinsic conductivity and high aspect ratio are widely used as conductive filler in stretchable flexible electronics. The elastic conductors using single wall carbon nanotube with printing techniques are introduced to fabricate flexible display. Stretchable active-matrix display was fabricated using printable elastic conductor and can survive over bending or crumpling due to its excellent electrical and mechanical property (Figure 1.2b, right).[17]

Unlike blending conductive composite, the conductive materials can be localized on the rubber substrate to maximize the electrical percolation network through transferring, spraying and dip-coating process (Figure 1.2c). With this process, even hydrophilic silver nanowire and conductive gel can also easily be deposited and infiltrated on the hydrophobic substrate. As a result, anisotropic conductive composite can be fabricated, which can be utilized strain sensors on the human skin (Figure 1.2d left), [18] transparent stretchable electrode (Fig, 1.2d middle),[19] stretchable circuit on the elastomer substrate (Figure 1.2d, right).[20] In the process of fabricated anisotropy stretchable conductor, fabrication of the conductive materials on the pre-strained substrate is facile, which impart more mechanical durability and insensitivity of mechanical deformation, thus, various sensors, biomedical electrode, and LED electrodes are employed pre-strain structure on the stretchable conductor.

On the other hand, the stretchable conductor is fabricated in a one directional fiber type to interconnect with other electronic devices (Figure 1.2e). Figure 1.2f, left shows wet spinning method that is the same method as the other polymer fiber made.[21] Polymer and conductive filler is blended and spinned out in the solvent to produce conductive fiber. The conductive fiber can be weaved into mesh electrode that impart high stretchability. Meanwhile, the conductive filer can be coated on the stretchable rubber fiber. Silver nanowire was dip-coated on the PU fiber and fixed with PDMS (Figure 1.2f, middle).[22] Pre-strained structure could also be applicable in here to help the stable electrical property under stretching and releasing of conductive stretchable fiber. Figure 1.2f right shows that CNT sheet was rolled up along with rubber fiber.[23] As the CNT sheet could be layered though multi-step process, the sandwich system of insulating layer between CNT electrode layers in fiber enabled to make mechanical actuator as well as stretchable conductive wire.

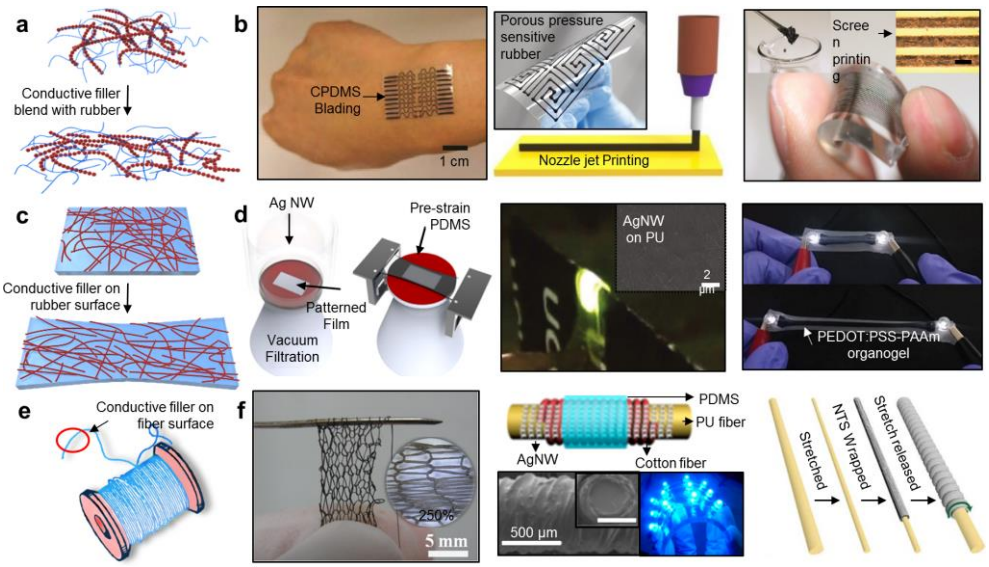

Figure 1.2 Strategy for stretchable conductor to enhance stretchability.

a) A schematic illustration of blending of conductive filler and polymer. b) Carbon black and PDMS was blended and patterned for skin mountable strain gauge (left)[15], Carbon nanotube (CNT) and PDMS was blended in hexane. Porous pressure sensitive rubber could be printed to make patterns of strain/pressure sensors (middle)[16], CNT and rubber gel composite was screen printed to produce an active matrix organic light emitting diods (right)[17]. Reproduced with permission. Copyright 2012, 2014, Wiley-VCH. Copyright 2009, Nautre Publishing Group. c) A schematic illustration of anisotropic stretchable conductor. d) Silver nanowires (Ag NWs) were filtered and the filtered Ag NWs film was transpired to pre-strained PDMS to fabricate strain sensor (left)[18], Ag NWs on polyurethane film used as electrode for polymer LED (middle)[19], PEDOT:PSS:PAAm organo gel was

coated on the rubber substrate (right)[20]. Reproduced with permission. Copyright 2015 American Chemical Society, Copyright 2013 Nature Publishing Group, Copyright 2015 Wiley-VHS e) A schematic illustration of stretchable conductive fiber. f) Knitted fabrics made form conductive stretchable fibers that consisted of Ag nanoparticle, CNT and poly(vinylidene fluorideco hexafluoropropylene) (left)[21], conductive composite fiber comprises cotton fabric with Polyurethane nanofilament core which absorbed Ag NW (middle)[22], Steps in the fabrication of carbon nanotube sheet (NTS) layered fiber. Additional functions such as mechanical actuators or stretchable conductor could be implemented by including other rubber and CNT sheath layers (right)[23]. Reproduced with permission. Copyright 2014, 2015 American Chemical Society, Copyright 2015 AAAS.

1.4. Applications of stretchable conductor using carbon based material and silver based materials

1.4.1 Skin-laminated piezoresistive strain sensors

Synthesized nanomaterials and their hybrids processed with established nanomaterials have enabled a variety of new sensors, including pressure, strain, and temperature sensing arrays. Exploiting the conductivity and/or piezoelectric properties of these nanomaterials in soft sensors in combination with unique mechanical and optical properties (*i.e.* stretchability and transparency) enables new biomedical applications. Carbon black, for example, has been widely utilized as a nano-filler for the conductive nanocomposite rubber (Figure 1.3a).[15] Patterned carbon black, in conjunction with the intrinsic softness of rubber materials, has led to novel piezoresistive strain sensor arrays in wearable formats for tracking motions and skin mechanical properties (left). The patterned conductive rubber intimately couples with skin at any location on the body, including joints, such as wrist and knee, for accurate monitoring of biomechanics (right). There are practical challenges in establishing contacts between functional 0D materials (*e.g.*, carbon black), however, which may result in reduced conductivity and higher power consumption. Percolations between 1D nanomaterials (*e.g.*, CNTs, NWs) are much more probable due to their high aspect ratio, leading to much higher conductivity even under stretched

states.[24-26] Figure 1.3b shows a porous pressure sensitive rubber-based structure composed of this kind of 1D CNT networks (left bottom),[16] which can be integrated as a pressure/strain sensor array (left top). The porous structure (made by using reverse micelle solutions) enhances sensitivity of the pressure/strain sensors further, while the percolated structure allows for large dynamic range (right).

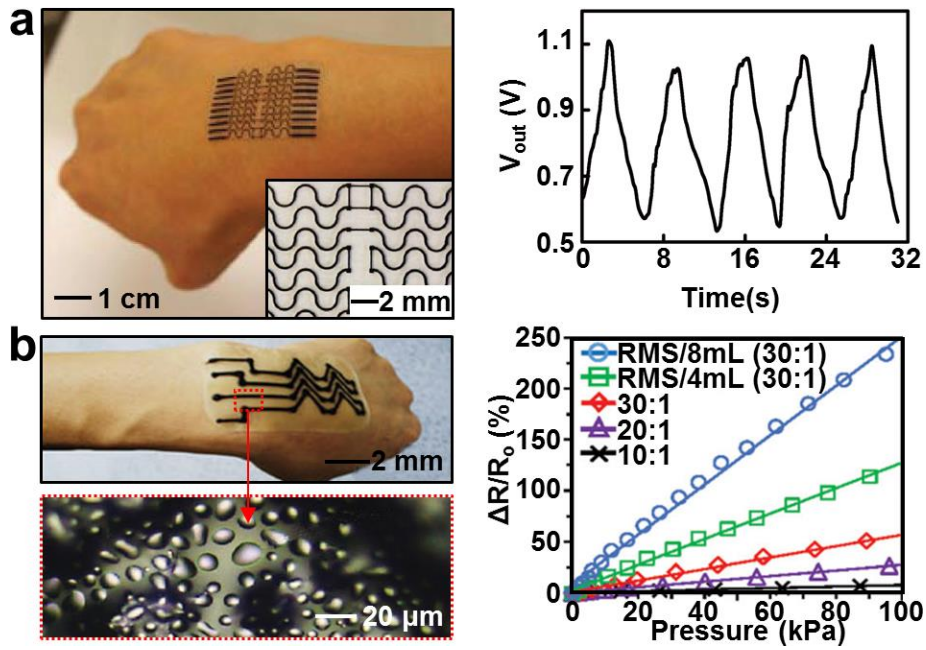

Figure 1.3 Skin-laminated piezoresistive strain sensors.

a) A photograph of a strain sensor array laminated on the human wrist to detect wrist motions (left). A graph of the output voltage under repeated wrist motions (right)[15]. b) A photograph of piezoresistive strain sensor fabricated with the printed CNT-PDMS nanocomposite (left top). A magnified view shows its porous structure (left bottom). The percent resistance change of the deformed CNT-PDMS nanocomposite with (blue, green) or without (red, purple, black) porous structure as a function of applied pressures (right)[16]. Reproduced with permission. Copyright 2016, WILEY-VCH Verlag GmbH & Co. KGaA, Weinheim

1.4.2 Implantable bioelectronics based on Carbon Nanotube

Flexible and stretchable bioelectronic devices consisting of unusual nanomaterials are applicable for invasive systems for monitoring internal organs. The signals captured from implantable bioelectronic devices are processed and trigger feedback commands to co-integrated therapeutic devices. Various unique properties of nanomaterials enable clinically relevant but previously unrealized functional modes, such as high quality electrophysiological mapping

Soft conducting carbon materials such as CNT fibers may also be applied to record electrophysiological signal from brain. Figure 1.4a shows CNT electrodes on the motor cortex of a mouse. The device detects high frequency single unit spikes with remarkably low impedance.[27] The high charge storage capacity of CNT fibers enables effective long term *in vivo* neural recordings. Au NPs assembled by layer-by-layer (LBL) methodologies on these types of electrodes further increases the charge storage capacity and forms high quality neural interface (Figure 1.4b).[28]

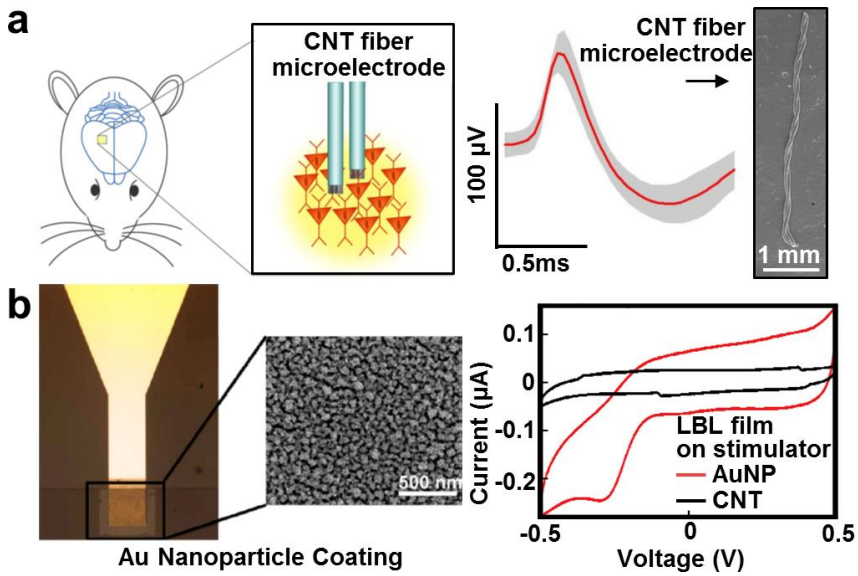

Figure 1.4 Implantable bioelectronics based on carbon nanotubes.

a) The SEM image of CNT microelectrode for recording brain signals (right) and the averaged neural waveforms recorded by the CNT microelectrode (left)[27]. b) Electrochemical characterization of a gold nanoparticle (red) and CNT (black) film assembled by the LBL method[28]. Reproduced with permission. Copyright 2016, WILEY-VCH Verlag GmbH & Co. KGaA, Weinheim

1.4.3. Stretchable electrode with silver nanocomposite

Since heat dissipation is largely dependent on line resistance in electronic system, the conductive materials should have high conductivity to enhance the performance in terms of speed and energy efficiency and prevent heat losses especially in interconnect and electrodes application. Unlike CNT nanocomposite, silver based nanomaterials have very high conductivity due to high conductivity of bulk silver (~10^6 S/cm), thus, there are many efforts to develop stretchable electrode itself using silver and rubber nanocomposite.

In fabrication of stretchable organic transistor active matrix, the word/bit line interconnection was printed with silver flake/ fluoropolymer composite ink (Figure 1.5a).[29] Silver flakes in elastomeric fluorine copolymer were localized by addition of fluorine surfactant and water with appropriate concentration. Therefore, the formation of conductive network on the surface of network led high stretchability and conductivity.

Also, most of the display application is based on interconnecting rigid lighting device with stretchable conductive rubber as interconnects. Figure 1.5b shows elastomeric polymer light-emitting device (EPLED) based on thin silver nanowires network embedded on the surface of poly(urethane acrylate) matrix.[19] The fabricated EPLED can emit light when it is uniaxially stretched to 120% strain and stably working at repeated stretching cycles.

1.4.3. Wearable energy supply devices based on nanomaterials silver based nanocomposite

As applications of soft bioelectronics expand, demand for more portable/wearable energy storage devices will also continue to increase. Nanomaterials and their hybrids have been actively used in these deformable energy harvesting and storage devices. In particular, the large surface area as well as the soft nature of nanoscale materials provides more reaction sites to generate and/or store energy with high mechanical deformability. These energy devices are conformally mounted on the human body, and can harvest and store energy from daily movements, sunlight, or residual heat, and supply it to the wearable/implantable bioelectronics systems.

Wearable piezoelectric energy harvesting devices have been demonstrated to generate electric power from the mechanical vibrations of daily movements. The elastic piezoelectric nanocomposite employing piezoelectric micro-particles (PMN-PT particles; lead magnesium niobate–lead titanate) and MWCNTs, mixed in a silicone rubber, generates electricity under mechanical stresses with stable output voltage and current (Figure 1.5c).[30] Ultra-long Ag NW networks as stretchable electrodes help to efficiently extract generated charges.

Photovoltaic energy harvesting devices represent another type of power

sources with continuous energy generation. To fabricate a solar cell as a wearable form, a functional fabric composed of CNT fibers coated with TiO_2 layers, perovskite, and P3HT/SWCNT/Ag NWs is developed (Figure 1.5d).[31] This flexible and fiber-shaped solar cell shows stable power generation performances and mechanical reliability under physical deformations, applicable to self-powering wearable energy supply modules.

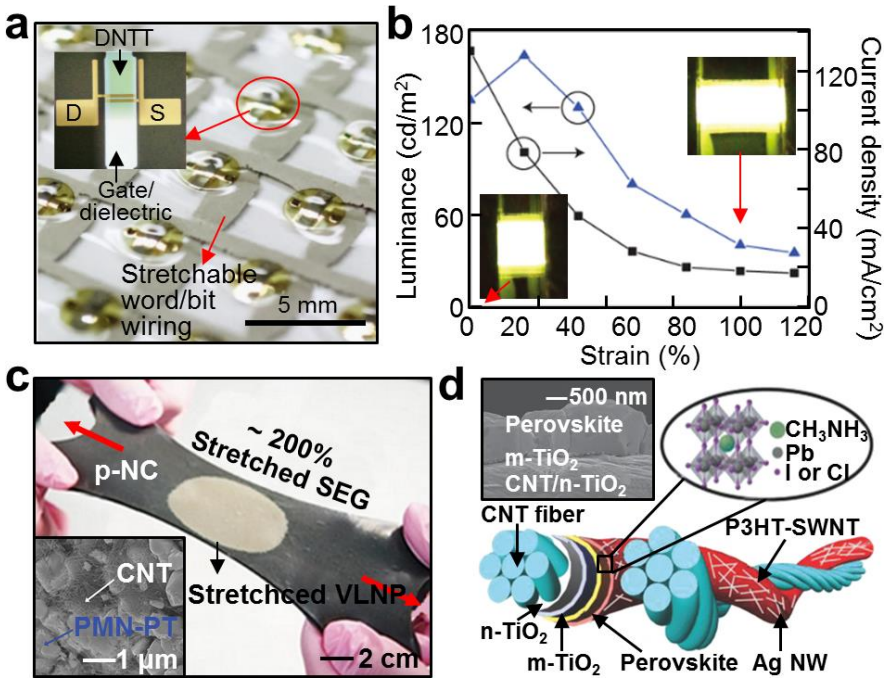

Figure 1.5 Stretchable electrode and energy devices using silver based stretchable conductor.

a) A photograph of magnified OTFT active matrix. Optical microscopic image of OTFT cell was shown in inset.[29] Reproduced with permission. Copyright 2015 Nature Publishing Group. b) Current density and luminance properties of a polymer light-emitting electrochemical cell at 12 V with increasing strain. Photographs of shows a PLEC biased at 14V 0 % and 100 % strains.[19] Reproduced with permission. Copyright 2013 Nature Publishing Group. c) An optical camera image of a stretchable piezoelectric nanogenerator. The inset shows good dispersion of piezoelectric microparticles and MWCNTs.[30] c) A schematic illustration of a CNT-fiber-

based perovskite solar cell. The SEM image shows cross-sectional view of the solar cell (inset).[31] Reproduced with permission. Copyright 2016, WILEY-VCH Verlag GmbH & Co. KGaA, Weinheim

1.5 Reference

(1) Park, J.; An, K.; Hwang, Y.; Park, J. G.; Noh, H. J.; Kim, J. Y.; Park, J. H.; Hwang, N. M.; Hyeon, T. *Nat. Mater.* **2004**, *3*, 891.

(2) Roduner, E. *Chem. Soc. Rev.* **2006**, *35*, 583.

(3) Munshi, A. M.; Dheeraj, D. L.; Fauske, V. T.; Kim, D. C.; Huh, J.; Reinertsen, J. F.; Ahtapodov, L.; Lee, K. D.; Heidari, B.; van Helvoort, A. T.; Fimland, B. O.; Weman, H. *Nano Lett.* **2014**, *14*, 960.

(4) Jung, S.; Lee, J.; Hyeon, T.; Lee, M.; Kim, D. H. *Adv. Mater.* **2014**, *26*, 6329.

(5) Kim, S.; Su, Y.; Mihi, A.; Lee, S.; Liu, Z.; Bhandakkar, T. K.; Wu, J.; Geddes, J. B., 3rd; Johnson, H. T.; Zhang, Y.; Park, J. K.; Braun, P. V.; Huang, Y.; Rogers, J. A. *Small* **2012**, *8*, 901.

(6) Paul, S.; Pearson, C.; Molloy, A.; Cousins, M. A.; Green, M.; Kolliopoulou, S.; Dimitrakis, P.; Normand, P.; Tsoukalas, D.; Petty, M. C. *Nano Lett.* **2003**, *3*, 533.

(7) Fan, Z.; Ho, J. C.; Jacobson, Z. A.; Yerushalmi, R.; Alley, R. L.; Razavi, H.; Javey, A. *Nano Lett.* **2008**, *8*, 20.

(8) Lipomi, D. J.; Vosgueritchian, M.; Tee, B. C.; Hellstrom, S. L.; Lee, J. A.; Fox, C. H.; Bao, Z. *Nat. Nanotechnol.* **2011**, *6*, 788.

(9) Kim, S.; Wu, J.; Carlson, A.; Jin, S. H.; Kovalsky, A.; Glass, P.; Liu,

Z.; Ahmed, N.; Elgan, S. L.; Chen, W.; Ferreira, P. M.; Sitti, M.; Huang, Y.; Rogers, J. A. *Proc. Natl. Acad. Sci. U.S.A.* **2010**, *107*, 17095.

(10) Kaltenbrunner, M.; White, M. S.; Glowacki, E. D.; Sekitani, T.; Someya, T.; Sariciftci, N. S.; Bauer, S. *Nat. Commun.* **2012**, *3*, 770.

(11) Kim, D.-H.; Ahn, J.-H.; Choi, W. M.; Kim, H.-S.; Kim, T.-H.; Song, J.; Huang, Y. Y.; Liu, Z.; Lu, C.; Rogers, J. A. *Science* **2008**, *320*, 507.

(12) Kaltenbrunner, M.; Sekitani, T.; Reeder, J.; Yokota, T.; Kuribara, K.; Tokuhara, T.; Drack, M.; Schwodiauer, R.; Graz, I.; Bauer-Gogonea, S.; Bauer, S.; Someya, T. *Nature* **2013**, *499*, 458.

(13) Kim, D.-H.; Choi, W. M.; Ahn, J.-H.; Kim, H.-S.; Song, J.; Huang, Y.; Liu, Z.; Lu, C.; Koh, C. G.; Rogers, J. A. *Appl. Phys. Lett.* **2008**, *93*.

(14) Fan, J. A.; Yeo, W. H.; Su, Y.; Hattori, Y.; Lee, W.; Jung, S. Y.; Zhang, Y.; Liu, Z.; Cheng, H.; Falgout, L.; Bajema, M.; Coleman, T.; Gregoire, D.; Larsen, R. J.; Huang, Y.; Rogers, J. A. *Nat. Commun.* **2014**, *5*, 3266.

(15) Lu, N.; Lu, C.; Yang, S.; Rogers, J. *Adv. Funct. Mater.* **2012**, *22*, 4044.

(16) Jung, S.; Kim, J. H.; Kim, J.; Choi, S.; Lee, J.; Park, I.; Hyeon, T.; Kim, D. H. *Adv. Mater.* **2014**, *26*, 4825.

(17) Sekitani, T.; Nakajima, H.; Maeda, H.; Fukushima, T.; Aida, T.; Hata, K.; Someya, T. *Nat Mater* **2009**, *8*, 494.

(18) Kim, K. K.; Hong, S.; Cho, H. M.; Lee, J.; Suh, Y. D.; Ham, J.; Ko, S. H. *Nano Lett* **2015**, *15*, 5240.

(19) Liang, J.; Li, L.; Niu, X.; Yu, Z.; Pei, Q. *Nature Photonics* **2013**, *7*, 817.

(20) Lee, Y. Y.; Kang, H. Y.; Gwon, S. H.; Choi, G. M.; Lim, S. M.; Sun, J. Y.; Joo, Y. C. *Adv Mater* **2016**, *28*, 1636.

(21) Ma, R.; Lee, J.; Choi, D.; Moon, H.; Baik, S. *Nano Lett* **2014**, *14*, 1944.

(22) Cheng, Y.; Wang, R.; Sun, J.; Gao, L. *ACS Nano* **2015**, *9*, 3887.

(23) Liu, Z. F.; Fang, S.; Moura, F. A.; Ding, J. N.; Jiang, N.; Di, J.; Zhang, M.; Lepro, X.; Galvao, D. S.; Haines, C. S.; Yuan, N. Y.; Yin, S. G.; Lee, D. W.; Wang, R.; Wang, H. Y.; Lv, W.; Dong, C.; Zhang, R. C.; Chen, M. J.; Yin, Q.; Chong, Y. T.; Zhang, R.; Wang, X.; Lima, M. D.; Ovalle-Robles, R.; Qian, D.; Lu, H.; Baughman, R. H. *Science* **2015**, *349*, 400.

(24) Lee, P.; Lee, J.; Lee, H.; Yeo, J.; Hong, S.; Nam, K. H.; Lee, D.; Lee, S. S.; Ko, S. H. *Adv. Mater.* **2012**, *24*, 3326.

(25) Xu, F.; Zhu, Y. *Adv. Mater.* **2012**, *24*, 5117.

(26) Sekitani, T.; Noguchi, Y.; Hata, K.; Fukushima, T.; Aida, T.; Someya, T. *Science* **2008**, *321*, 1468.

(27) Vitale, F.; Summerson, S. R.; Aazhang, B.; Kemere, C.; Pasquali, M. *ACS Nano* **2015**, *9*, 4465.

(28) Zhang, H.; Shih, J.; Zhu, J.; Kotov, N. A. *Nano Lett.* **2012**, *12*, 3391.

(29) Matsuhisa, N.; Kaltenbrunner, M.; Yokota, T.; Jinno, H.; Kuribara, K.; Sekitani, T.; Someya, T. *Nat Commun* **2015**, *6*, 7461.

(30) Jeong, C. K.; Lee, J.; Han, S.; Ryu, J.; Hwang, G. T.; Park, D. Y.; Park, J. H.; Lee, S. S.; Byun, M.; Ko, S. H.; Lee, K. J. *Adv. Mater.* **2015**, *27*, 2866.

(31) Li, R.; Xiang, X.; Tong, X.; Zou, J.; Li, Q. *Adv. Mater.* **2015**, *27*, 3831.

Chapter 2. Stretchable Heater Using Ligand-Exchanged Silver Nanowire Nanocomposite for Wearable Articular Thermotherapy

2.1 Introduction

Joints in the human body are frequently injured due to obesity, occupational overuse, or aging. The joint injuries tend to cause many symptoms such as pain, swelling, muscle weakness, and numbness.[1–5] The thermal therapy is one of the classic physiotherapies used in orthopedics to alleviate these symptoms. Its physiological effects include thermal expansion of the vascular systems (increased blood flow) and their surrounding collagen tissues, thereby relieving pain and reducing joint stiffness.[6,7] There are several conventional heat therapy methods, such as heat packs or wraps:[8,9] the heat packs are heavy and bulky, and another downside is that it is difficult to control their temperature; the heating wraps, whose temperatures are controlled by the joule heating of electrodes and resistors, are relatively thin but their wearability is still an issue mainly caused by their mechanical rigidity and weight. While continuous point-of-care thermal treatments maximize the therapeutic effects, the technical drawbacks of currently available heat wraps and packs limit their uses

mostly in hospitals. Consequently, the development of the stretchable and wearable heating devices in a portable form is highly desired.

To date, there have been diverse studies about stretchable electrodes that can be used as heating elements based on the joule heating. Outstanding examples are stretchable metal nano-material based electrodes[10–12], using carbon nanotubes (CNTs) embedded in elastomers,[13,14] in a polymeric media,[15,16] silver reduction precursor electrospun rubber fibers with percolation of silver nanoparticles[17] gold nanosheet electrode on a rubber substrate,[18] and gold-nanoparticle-based stretchable conductor.[19] Although each of them has demonstrated some kind of interesting feature, a cheap and simple conductive elastomer that can be easily patterned and processed is still required to be developed. Silver nanowires (Ag NWs) have been recognized as a potential candidate[20–22] because they have higher conductivity than CNTs, and are cheaper than gold. Their one-dimensional wire structure is better to form electrical percolation networks than particles or flakes, and can maintain good conductivity under deformation, especially when stretched. However, an aqueous solution of as-synthesized Ag NWs cannot be mixed homogeneously with many organic-phase elastomers. In the previous applications, Ag NW networks were filtrated and transferred[20] or Ag NWs were dip-coated and sprayed on substrate,[23,24] in which the post-deposition processing to define various patterns was difficult.

Here, we present a soft and stretchable heating element that is lightweight and thin, and is conformally integrated with the human joints and the skin for effective heat transfer and thermotherapy. The heater is composed of highly conductive Ag NW/elastomer nanocomposite. The ligand exchange (LE) of Ag NWs allows the nanowires to be homogeneously dispersed in the elastomeric media, and the excellent homogeneity leads to mechanically and electrically uniform characteristics and processability of the composite into various patterns, which enables reliable, large-area heating over the entire joint surfaces. The heater is operated by a custom-made electronic band equipped with a battery, a microcontroller, and other circuits, allowing users to remain mobile. The softness of the heater provides maximum comfort, system robustness, and effective thermo-therapies even under joint flexion or muscle extension.

2.2 Experimental Section

2.2.1 Synthesis of Ag nanowires

Polyol process was used to synthesis Ag NW. First, 100ml of ethylene glycol (EG) was heated at 153^{o}C in oil bath. When the temperature of EG was saturated, 30ml of 0.147M PVP (MW 55,000; Aldrich, USA) solution in EG was added. 30 mL of 0.094 M silver nitrate ($AgNO_3$; > 99% purity, Strem Chemicals Inc., USA) in an EG solution was injected with 72 ml/hr,

10 minutes after 800 μL of a 4 mM copper chloride solution ($CuCl_2 \cdot 2H_2O$; Aldrich, USA) was added. 10 mins later, the synthesis reaction took 80 mins including injection time.

2.2.2 Preparation of Ag NW/SBS nanocomposite

Ligand exchanged Ag NW was dispersed in toluene with 50 mg/ml concentration. 1:10 weight ratio of SBS (KTR-101, Kumho, South Korea) was dissolved in toluene. Each solution was mixed with appropriate ratio and dried at 55^{o}C on the hotplate to make LE Ag NW/SBS nanocomposite.

2.2.3 Characterizations of LE Ag NWs

Fourier-transform infrared (FTIR) spectra were obtained in the transmission mode using the FTIR spectorometer (FT-IR 200, Jasco, USA). The contour map of sheet resistance was measured using the automatic resistivity meter (FPP-5000 4-point probe, Changmin, Co., South Korea). The cross-sectional images were obtained by a scanning electron microscope (SEM; JSM-6701F, JEOL, Japan). The stress–strain curve was measured with a 2 cm × 2 cm heater, using the universal testing machine (Instron5543, Instron, USA).

2.2.4 Fabrication of stretchable heater

To produce the heating layer of the stretchable mesh heater, the LE Ag

NW/SBS nanocomposite solution was cast on a serpentine-patterned PDMS mold with 300-μm line width and then dried at 60 °C. The encapsulation layer of the heater was formed by the SBS solution cast on a 400-μm line patterned PDMS mold. After heating and the encapsulation layer was de-molded, each layer was aligned on the 400-μm patterned PDMS mold and placed on a 130 °C hotplate for 30 min to weld them to each other. The other side of the encapsulation layer was assembled as well after wiring both ends of the mesh with copper wires and conductive paste. The whole size and pattern size of the mesh for wrist band were modified according to the wrist size.

2.2.5 Characterizations of the stretchable mesh heater

The relative resistance under tensile strain were obtained by a parameter analyzer (B1500A, Agilent, USA) with a custom-made *x*-axis motion stage. All thermal properties and images were obtained by an infrared (IR) camera (Thermovision A320, FLIR system, Sweden). The average and maximum temperature were analyzed using the built-in analysis software (FLIR tools, FLIR system, Sweden).

2.2.6 Finite-element analysis (FEA) of electrical conduction of the heater

The Ag NW/SBS nanocomposite was conductive because the Ag NWs

formed a conduction network. When the nanocomposite was subjected to an external load, the partial disconnection of the conduction network and the piezoresistivity of the Ag NWs increased the overall resistance of the composite. Finite-element simulations were used to analyze the electrical conduction and resistance change of the heater during stretching (Figure 2.6b). The stretching and electrical conduction were solved sequentially: the mechanical stretching problem was solved first, and then the electrical conduction was solved using the deformed configuration and the strain distribution. A repeating unit of heating elements was modeled using six- and eight-node solid elements. The heating element was composed of two layers: the 50-μm-thick Ag NW/SBS composite was placed on the 150-μm-thick SBS layer. For comparison, three different concentrations of Ag NWs in the nanocomposites were considered. For the mechanical finite-element simulation, the incompressible neo-Hookean model was used to represent the SBS and Ag NW/SBS nanocomposite layers:

$$W = C_1 (I_1 - 3) \quad \text{(S6)}$$

where W is the strain energy potential, I_1 is the first invariant of the left Cauchy–Green tensor, and C_1 (= 0.35, 19.73, 52.03, and 125.3 MPa for SBS, 9, 13, and 18 vol% Ag NW/SBS nanocomposites, respectively) is a material parameter. Periodic boundary conditions were imposed on the sides of the finite-element models. Stretching occurred mainly in the serpentines in the mechanical loading direction (Figure 2.4b), and the strain distribution did

not show much difference with variations in the Ag NW concentration. Using the deformed configuration and the strain distribution, the electrical conduction in the heating element was calculated. The resistivity of the Ag NW/SBS nanocomposites was assumed to vary with deformation, following the relationship:

$$(\rho - \rho_0) / \rho_0 = C_\rho (I_1 - 3)^n \quad \text{(S7)}$$

where ρ and ρ_0 are the resistivities of the initial and deformed states, respectively; C_ρ and n are material parameters obtained by fitting Eq. (S7) with the measured resistance-strain curves of bulk nanocomposites. The value of C_ρ was 93.01, 21.72, and 1.272 for the 9, 13, and 18% Ag NW/SBS nanocomposite, respectively. The value of n was 0.686, 0.633, and 0.74 for the 9, 13, and 18% Ag NW/SBS nanocomposite, respectively. For the heating element made of the 9% Ag NW/SBS nanocomposite, the serpentines aligned in the mechanical-loading direction reduced the conductivity because they were more stretched (Figure 2.7c). For the heating element made of the 18% Ag NW/SBS nanocomposite, the decrease in conductivity was negligible because the resistivity of the 18% Ag NW/SBS nanocomposite was less sensitive to deformation. This was because the composite with higher Ag NW concentration had more conductive paths than that with lower concentration, and therefore the resistivity was less affected by the destruction of conductive paths. For a given electric potential difference, the current flowing in the heating

element was calculated, which yielded the overall resistance of the heating element (Figure 2.6b).

2.2.7 Irritation test

Irritation test was performed by comparision of pictures of naked skin before and after applying the mesh heater. The mesh heater was put on the upper wrist of each person, wrapped and fixed with gauze and tape and kept for 12 hours. After 12 hours, pictures of the wrists of the subjects were taken (Figure S5). The subjects (age: 25 ~ 35 years) were all coauthor and all work involved informed consent from the subjects.

2.2.8 Custom-designed electronic band and its operation

One of the batteries (Li–polymer, 3.7 V) in the electronic band was used to operate the microcontroller unit (MCU; Arduino mini pro 5.0V, Arduino, Italy). The on–off pattern signal from the MCU board induced an effective voltage (V_{eff}) applied to a transistor (Figure 2.11b) The drain–source resistance of the transistor ($R_{eff,tr}$) was modulated according to the duration of the on-signal (duty cycle), and the temperature of the heater was controlled with the other battery (V) for joule heating as follows:

$$V_{eff} = I \times R_{eff,tr} \quad \text{by Ohm's law (S1)}$$

$$\frac{V - V_{heater}}{R_{eff,tr}} = I \quad \text{(S2)}$$

$$Q_{heater} \propto I^2 \times R \qquad \text{by Joule's first law (S3)}$$

$$Q_{\mathrm{heater}} \propto \left(\frac{V - V_{\mathrm{heater}}}{R_{\mathrm{effd,tr}}}\right)^2 \times R \qquad \text{(S4)}$$

$$Q_{\mathrm{heater}} \propto \left\{\frac{V_{\mathrm{eff}}(V - V_{\mathrm{heater}})}{I}\right\}^2 \times R \qquad \text{(S5)}$$

Since the effective voltage was proportional to the duty cycle, the higher duty cycle released more heat through the heater.

2.2.9 Finite-element analysis (FEA) of heat transfer from the heater to the human body

Finite-element simulations were used to analyze the temperature distribution underneath the skin during heating (Figure 2.12). The heaters and tissues were modeled using six- and eight-node solid elements. The heating element was composed of three layers: the 50-μm-thick Ag NW/SBS composite was sandwiched between 150-μm-thick SBS layers. A repeating unit of heating elements was placed on the epidermis under which the dermis, fat layer, and muscle layer were located. The density, heat capacity, thermal conductivity, and thicknesses of the heater and tissue layers are listed in Table S1. For comparison, the heater stretched by 30% was also modeled.

Table S1

Material or Tissue	Density ($g \cdot cm^{-3}$)	Heat capacity ($J \cdot g^{-1} \cdot °C^{-1}$)	Thermal conductivity ($W \cdot m^{-1} \cdot °C^{-1}$)	Thickness (mm)
Ag NW/SBS composite	3.254*	0.779*	77.34*	0.05
SBS	1.665	0.897	0.18	0.15
Epidermis[1]	1.2	3.6	0.24	0.08
Dermis[1]	1.085	3.68	0.47	1.7
Fat[1]	0.85	2.3	0.16	5.8
Muscle[1]	1.085	3.768	0.42	19

* estimated by the rule of mixture

Periodic boundary conditions were imposed on the sides of the finite element models. The temperature of the bottom of the muscle layer was kept constant at 36.5 °C, whereas heat was convected and radiated to the surrounding air on the exposed surfaces of the epidermis and the device with a film coefficient of 9.75 $W \cdot m^{-2} \cdot °C^{-1}$. The initial temperature distribution was obtained by solving the steady-state heat-transfer problem, shown in Figure S6. With the power supply, heat was generated in the Ag NW/SBS composite at a specific-heat generation rate of 0.02 $W \cdot mm^{-3}$, and the temperature evolution was calculated by solving the transient-heat-transfer problem.

2.2.10 Blood flow measurement

To understand the thermodynamic effect of thermo-therapy, blood flows from five healthy adult volunteers were characterized using echocardiography. The right arm was fixed under the sitting position and the right radial artery was scanned (Accuvix V10, Samsung Medison CO., Ltd, Korea) in the longitudinal direction at the wrist. All volunteers took a 10-min rest before the blood-flow measurement, and the blood flow was measured after the heater was switched on for 10 min. The peak systolic velocity (PSV) and end-diastolic velocity (EDV) of the radial artery were estimated in the pulsed-wave Doppler mode. The five subjects (age: 25 ~ 35 years) were all coauthor and all work involved informed consent from the subjects.

2.3 Result and Discussion

Ag NWs are synthesized with modified polyol process.[25,26] The Ag NWs are initially dispersed in a dimethylformamide (DMF) due to the polyvinylpyrrolidone (PVP) ligands. To accomplish stable, uniform, and rapid heating under repeated mechanical strain,[27,28] homogeneous composite of Ag NWs and polymer is important. However, most elastomeric polymer can be only dissolved with nonpolar solvents. In order to make homogeneous mixture of Ag NWs and solution state elastomer, ligand

exchange (LE) reaction is necessary. Figure 2.1a shows schematic illustration of LE process.[30] Among various elastomers, poly(styrene–butadiene–styrene) (SBS) thermoplastic rubber which has physically cross-linking is used to make high conductive homogeneous composite.[29] Figure 2.1b shows scanning electron microscope (SEM) image of mixture of LE Ag NWs and SBS elastomer. The exchanged surface of Ag NWs are characterized by Zeta-potential measurements, FTIR spectra, thermogravimetric analysis (TGA).

The LE Ag NWs with hexylamine ligand have higher conductivity than the PVP ligand Ag NWs after drying at room temperature due to the short chain length of Hexylamine, thereby, the contact resistance between Ag NWs is lower than Ag NWs with PVP ligands. This property also influences the conductivity of Ag NWs / SBS composites although low annealing temperature is conducted. The physically cross-linked elastomer like SBS has advantage on a the high loading of LE Ag NWs compored to chemically cross-linked one like polydimethylsiloxane (PDMS), thus the conductivity of AgNWs nanocomposite can be maximized. The conductivity of the LE-Ag NW/SBS nanocomposite starts to be saturated from ~20 vol%, which is a selected volume ratio for the next processes. The ligand exchanged Ag NW distributed homogeneously in the LE-AgNW/SBS nanocomposite, thereby, the nanocomposite with ligand exchanged Ag NW showed homogeneous sheet resistance distribution compared to that of unexchanged

Ag NW nanocomposite (Figure 2.2). The SEM images also confirm the homogeneous LE-Ag NW/SBS composite with corresponding region.

Maximizing the system-level softness/stretchability makes conformal integration of the heater on movable joints and provides highest comfort and efficient heat conduction.[30] Considering this, we adopted fully serpentine mesh designs.[31] A schematic illustration shows the fabrication process using serpentine designed PDMS molds (Figure 2.3a).[32] Since the Ag NWs are dispersed in toluene after LE, the contact angle of the LE Ag NWs on the PDMS mold is smaller, indicating that the wettability of LE Ag NWs is better than non-exchanged NWs, which is advantageous for the molding process (Figure 2.3b). The heating layer (LE-Ag NW/SBS nanocomposite) is inserted between the insulation layers and pressed on the hot plate at 130 °C (Figure 2.4a), which forms the final serpentine mesh heater after welding the layers.[33] A SEM image with colorized cross-section shows the good interfaces (Figure 2.4b). In terms of the mesh design, the higher fill factor is beneficial for more efficient heat transfer (Figure 2.5),[34] and it does not diminish the stretchability in the biaxial directions (Figure 2.4c).

Figure 2.4d shows the changes in the temperature–time profiles when various input voltages are applied to the mesh heater for ~120 s. Because of the high conductivity, the temperature can be rapidly increased from room temperature to ~40 °C with only an applied voltage of 1.0 V. The stable and fast heating property of the mesh heater is also confirmed by the repetitive

on–off cycles with durations of ~60 s under an applied voltage of 0.5 V (Figure 2.4e).

Figure 2.6 shows the electrical, mechanical, and thermal characterization of the heaters. Compared with the film-type SBS encapsulation (Figure 2.7a, left), the patterned SBS encapsulation (Figure 2.7a, right) induces less stress during stretching regardless of the mixing ratio of LE-Ag NW/SBS (18/82 and 13/87) (Figure 4a; black versus red and blue lines). The concentration of LE-AgNW in SBS elastomer do not also affect the strain distribution, which is explained by the finite element (FE) simulation (Figure 2.7b). However, the ratios of LE-Ag NW/SBS in the heating layer have much influence on the thermo-resistive properties. The elative resistance (R/R_0) changes while stretching the mesh heaters depending on the LE-Ag NW concentrations were measured (Figure 2.6b). The higher LE-Ag NW concentration of mesh heater shows more stable resistance under strains because of less disconnections of conducting paths, which is confirmed by the FE simulations of electrical conduction of the stretched mesh heaters (Figure 2.7c; see Experimental section for details).

As for the wearable systems applied in the articular region, the devices should endure the deformation of joints. The strains induced on the wrist and the knee during flexion or extension are ~17 and ~26% (Figure 2.8a and b), respectively, which are much below ~50%. Based on these observations, the maximum temperature change is measured in the strain range of ~50%

and below (Figure 2.6c). A high concentration of LE-Ag NWs in the mesh heater (e.g., LE-Ag NW:SBS = 18:82 in volume ratio) leads to the low resistance, high current flow, and thus high temperature at the same applied voltage, and vice versa for the mesh heater with low concentration of LE-Ag NWs (e.g., LE-Ag NW:SBS 9:91 in volume ratio). As the heater is stretched and the gaps between serpentine lines are expanded, the surface temperature slightly decreases owing to the increased exposure to ambient air that cools down the mesh surface. We choose the LE-Ag NW/SBS mesh with 18/82 vol% to test cyclic stretching performance, which shows stable resistance and joule-heating performance under ~30% strain (Figure 2.6d). Figure 2.6e shows a series of infrared (IR) camera images during the joule heating at an applied voltage of ~0.75 V under uniaxial strains of ~0, ~20, ~40, and ~60%. The air-cooling effect in Figure 2.6c is also observed in Figure 2.6e.

When a large-area stretchable mesh heater (14 cm × 6.5 cm; Figure 2.9a, left) is integrated with a custom-made electronic band (Figure 2.9a, right), the system becomes portable. The heater size matches the average wrist size of the adult subjects. The mesh heater is safe to use and the test subject shows no rashes or signs of irritation after wearing it for 12 h (Figure 2.10a and b). Powered by the battery installed in the electronic band, the entire area of the stretchable mesh generates heat. The properties of homogeneity, high conductivity, and softness enable the stretchable heater to heat evenly and maintain conformal contacts with the joint during flexion and extension

(IR camera images in Figure 2.9b). The conducting layer sandwiched between the thin elastomeric encapsulation layers prevents electrical leakage but transfer heat effectively. Figure 2.9c shows a schematic illustration and the corresponding circuit diagram of the electronic band containing the power supply and the microcontroller unit (MCU). A custom-designed program is installed in the MCU to control the heating modes (Figure 2.11a). The number of clicks on the switch determines the specific heating mode by modulating the voltage applied to the gate terminal of the transistor through pulse-width modulation (Figure 2.11b; see Experimental section for details). The transistor resistance is modified by changing the gate voltage, which controls the electrical current to flow through the heater. Various thermal profiles can be either custom-designed or pre-programmed (Figure 2.9d). The custom-designed program also would turn the power switch off automatically after 30 min of the operation in order to prevent low-temperature burns (right end of Figure 2.9d).

Articular thermotherapy induces vasodilation and increases blood flow around the joints, which reduces pain and joint stiffness.[7,35] In order to achieve adequate therapeutic results, the effective heat transfer from the mesh heater is important. Heat transfer modeling from the mesh heater shows that the overall temperature rises on the skin surface and in the subcutaneous layer by thermal diffusion (Figure 2.12 and 2.13a; see Experimental Section in detail).[36] The stretched mesh under the flexed

condition (ε = 30%) continues to effectively heat the subcutaneous layer (Figure 2.13b). The degree of vasodilation, one of the effects of the thermal therapy, is to be estimated by directly measuring blood flow in the radial artery with B-mode ultrasound (Figure 2.14a and b).[37] Five healthy adult volunteers participated in the test. The color Doppler imaging (Figure 2.14c) displays the pulsatile blood flow in the radial artery. The dynamic indices, including the peak systolic velocity (PSV) and the end-diastolic velocity (EDV), are measured directly from the Doppler spectral waveforms at the baseline (initial) and after heating (~40 °C) for 10 min (Figure 2.14d). Warming by the stretchable heater increases PSV from 54.02 ± 1.65 to 60.22 ± 0.96 cm/s (n = 5, P < 0.05; Figure 6c, left) and EDV from 11.28 ± 1.63 to 14.54 ± 1.22 cm/s (n = 5, P < 0.05; Figure 2.14d, right). These results demonstrate the blood flow increase by the articular thermal actuation, possibly leading to the pain alleviation and the muscle relaxation.[35,38]

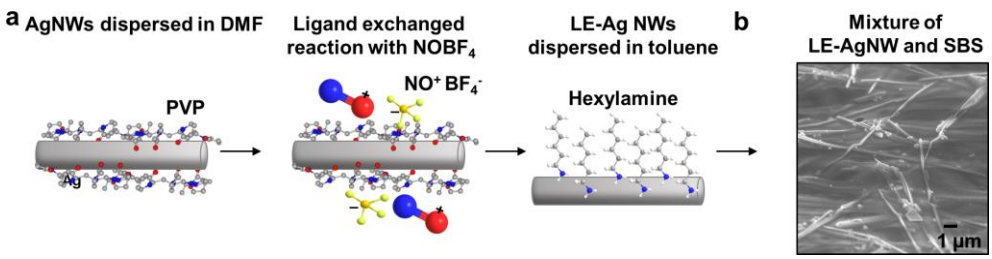

Figure 2.1 Ligand exchange of silver nanowire (LE-AgNW) and LE-AgNW/SBS composite.

(a) Schematic illustration of the ligand-exchange reaction for silver nanowires. (b) SEM image of LE-AgNW/SBS composite.

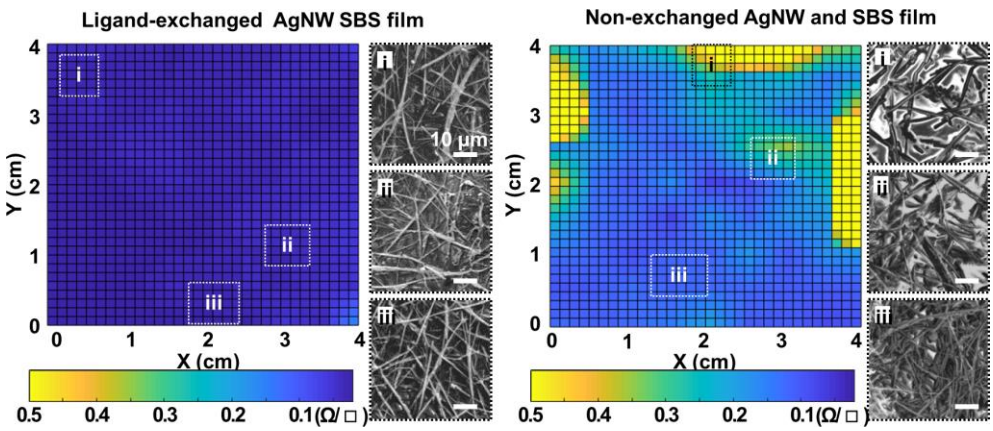

Figure 2.2 The contour maps of nanocomposites before and after ligand exchange Ag NW.

Maps obtained by interpolation of sheet resistance from 5 by 5 points. SEM images are corresponding to each regions from the maps.

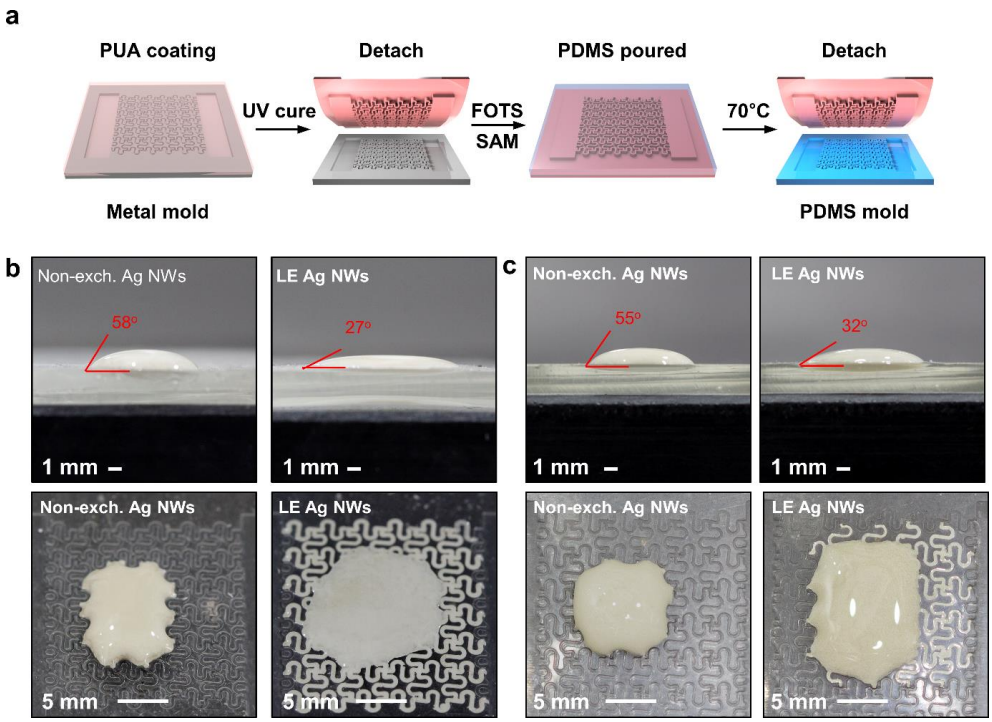

Figure 2.3 PDMS mold fabrication and its effects.

(a) Schematic illustration showing the fabrication process of PDMS mold with serpentine design. (b) (Top) Contact angles of non-exchanged Ag NWs dispersed in dimethylformamide and LE Ag NWs dispersed in toluene on the PDMS substrate. (Bottom) Comparison of wetting properties of both solutions on the PDMS mold. LE Ag NWs show the better wetting. (c) (Top) Contact angles of non-exchanged Ag NWs and LE Ag NWs after mixing with SBS on the PDMS substrate. (Bottom) Comparison of wetting properties of both solutions after mixing with SBS on the PDMS mold. LE Ag NW/SBS shows better wetting properties.

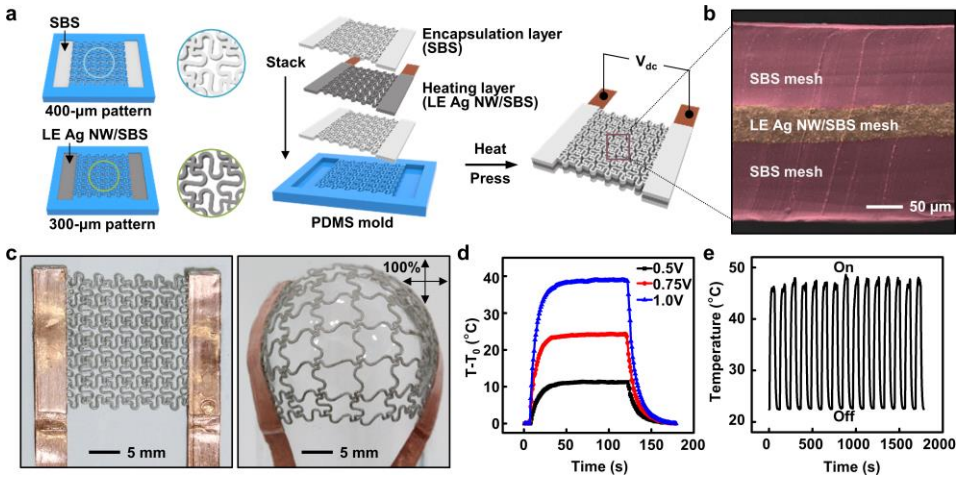

Figure 2.4 Fabrication of mesh heater and heater performance.

(a) Schematic illustration of the mesh heater fabrication process. The stretchable heater consisted of encapsulation layers (SBS) and a heating layer (LE Ag NW/SBS). Thermal welding with heat and pressure was used to combine and bond each layer. (b) SEM images showing the welded interfaces. (c) Optical image of a final mesh heater (left) before and (right) after biaxial stretching up to ~100%. (d) Temperature profiles under applied voltages of 0.5, 0.75, and 1.0 V on the heater. (e) Stable and fast on/off responses under applied voltage of ~0.5 V.

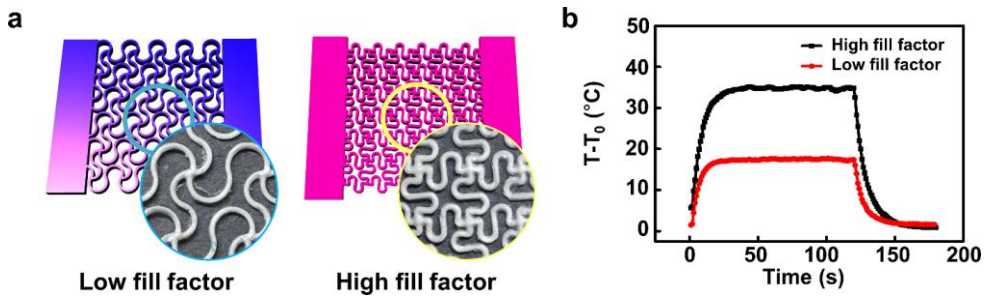

Figure 2.5 Serpentine mesh design effect.

(a) Mesh designs with (left) low fill factor and (right) high fill factor. (b) Temperature–time profiles for mesh designs with different fill factors.

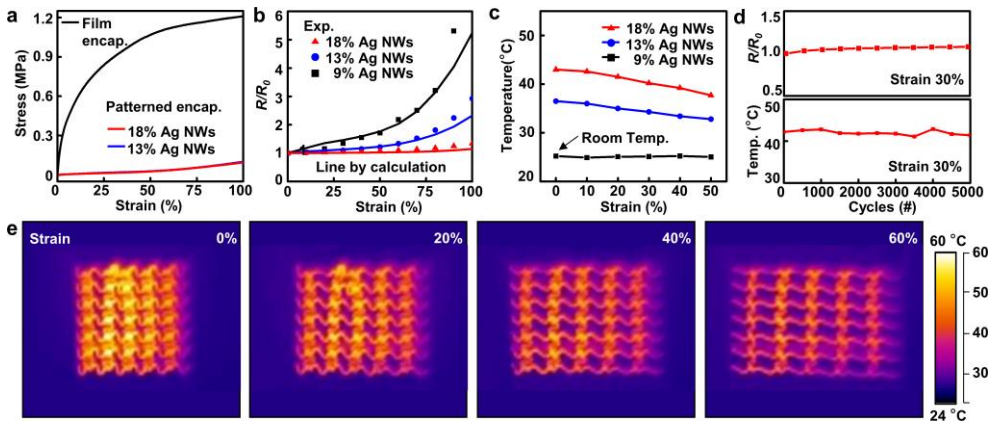

Figure 2.6 Charaterizations of mesh heater.

(a) Stress–strain curves of mesh heaters depending on the encapsulation type and Ag NW concentration in the LE Ag NW/SBS mesh layer. Each encapsulation type is illustrated by a photograph in Figure S4a. (b) Experimental (dot) and theoretical (line) values of relative resistance (R/R_0) of LE Ag NW/SBS meshes with different amounts of Ag NWs under tensile strains up to ~100%. (c) Temperature profiles of LE Ag NW/SBS meshes with different amounts of Ag NWs under tensile strains up to ~50% under applied 0.45V. (d) Cyclic stretching test with applied strain of ~30%. The changes in (top) relative resistance and (bottom) temperature were monitored in the LE Ag NW/SBS mesh with volume ratio of 18/82. (e) Infrared (IR) camera images of meshes at applied strains of 0, 20, 40, and 60% and applied voltage of 0.75 V.

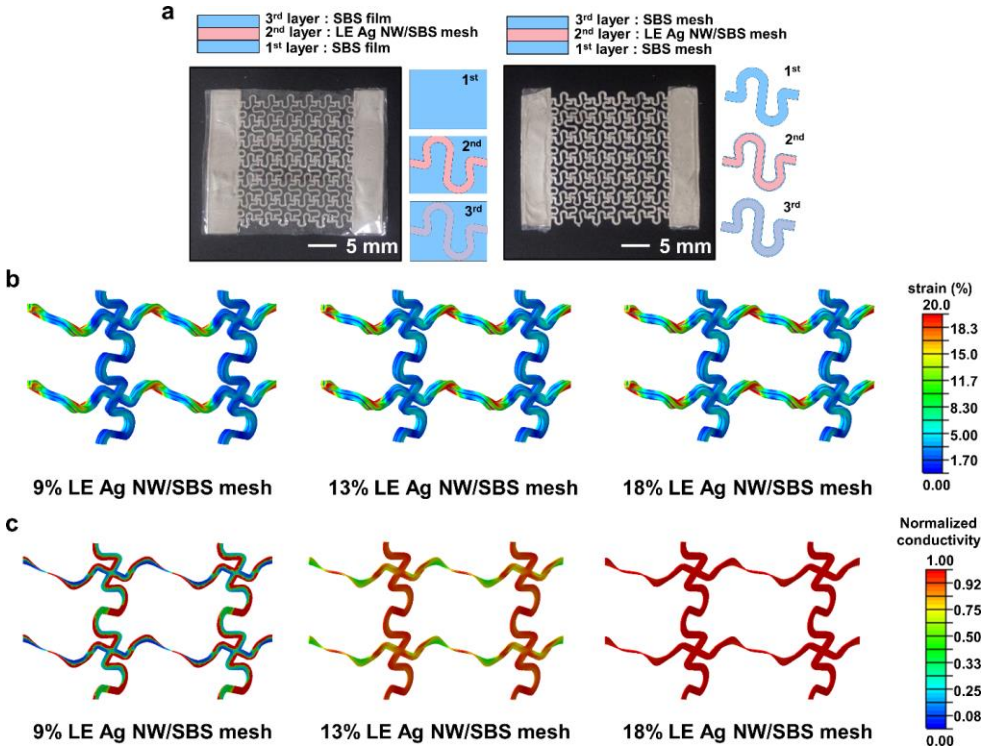

Figure 2.7 Mechanical and electrical characterization of mesh heater.

(a) Images and schematic illustrations of different encapsulation types: (left) film; (right) patterned. The mesh-type heating layer of LE Ag NW/SBS was sandwiched by encapsulation layers. (b) Finite element (FE) simulation of strain distribution at applied strain of 60%. (c) FE simulation of the normalized conductivity of mesh stretched by strain of 60%.

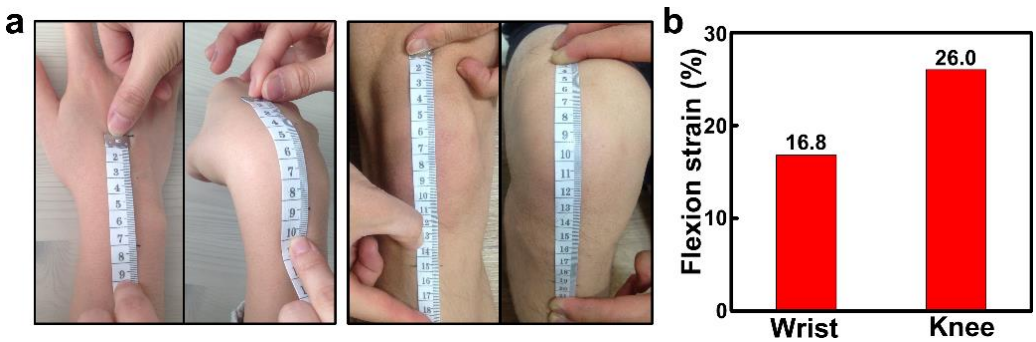

Figure 2.8 Strain anaysis from various joints.

(a) Measurement of induced strain in flexion and extension of (left) wrist and (right) knee. (b) Graph showing the averaged induced strain on wrist and knee (n = 4).

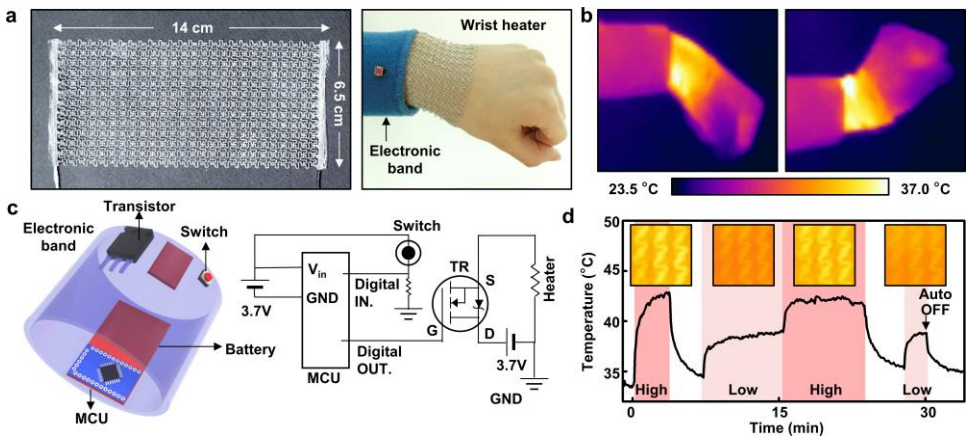

Figure 2.9 Application for thermotherapy.

(a) (Left) Image of a large-area stretchable heater designed for the wrist; (right) image of the heater as it was worn on the wrist. The blue strap shows the custom-made electronic band for the power supply and electronic circuits. (b) IR camera images when the wrist moved downward and upward. (c) Schematic illustration showing (left) components of the electronic band and (right) the corresponding circuit diagram. (d) Control of temperature profiles using a custom-made program; the insets show IR camera images obtained under each heating condition.

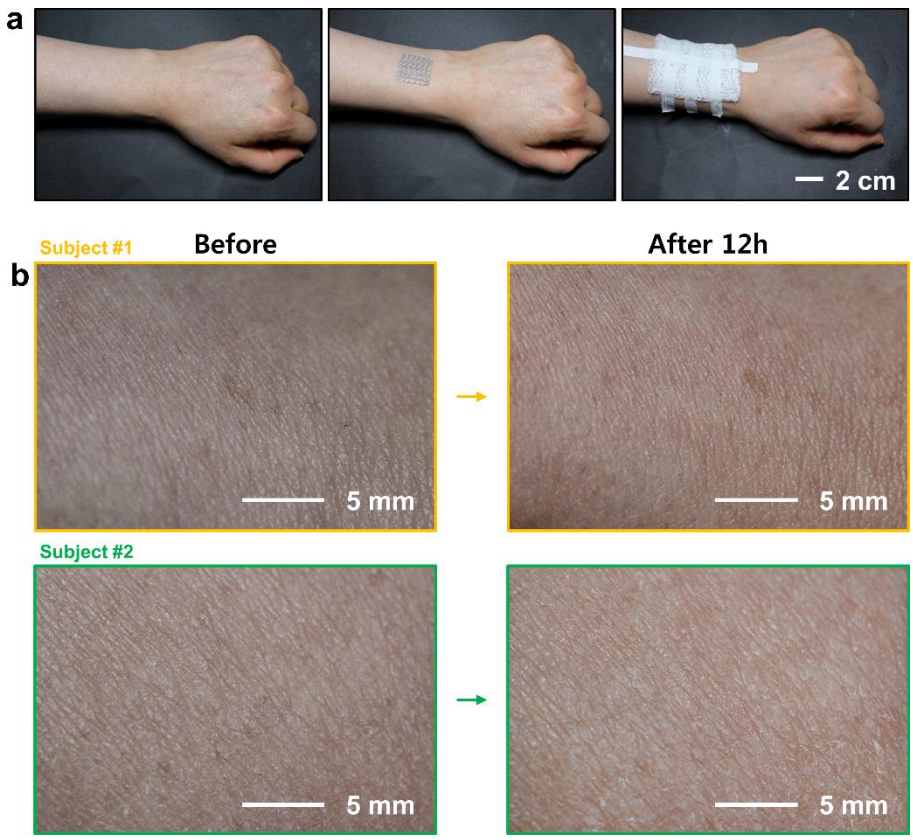

Figure 2.10 Irritation test.

(a) Images showing the skin irritation test: the mesh heater was placed on upper wrist and fixed in place using gauze and tape for 12 h. (b) Images of skin (left) before and (right) after irritation treatment of two subjects.

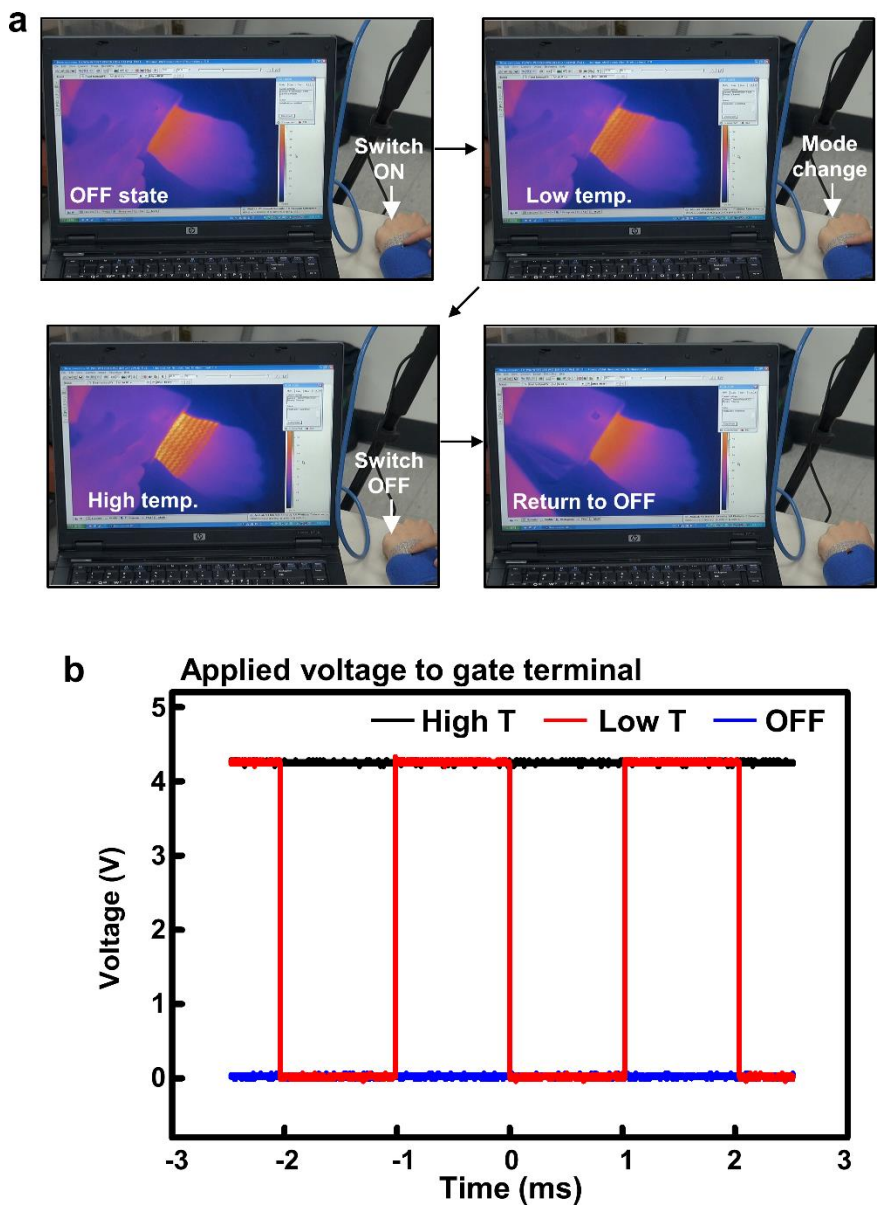

Figure 2.11 Integration of customized electronic band.

(a) A custom-designed program was operated by clicking the switch. (b) Changes to the voltage applied to the gate terminal of the transistor in the electronic band.

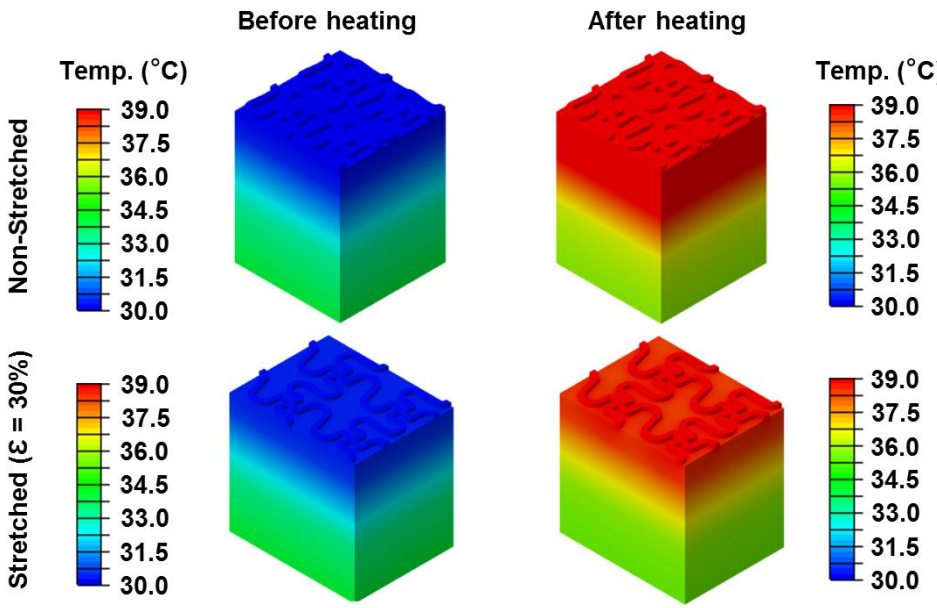

Figure 2.12 Computer simulation of heat diffusion.

Simulation of three-dimensional temperature distribution from the mesh heater to the subcutaneous layer before heating and after 15 min of heating.

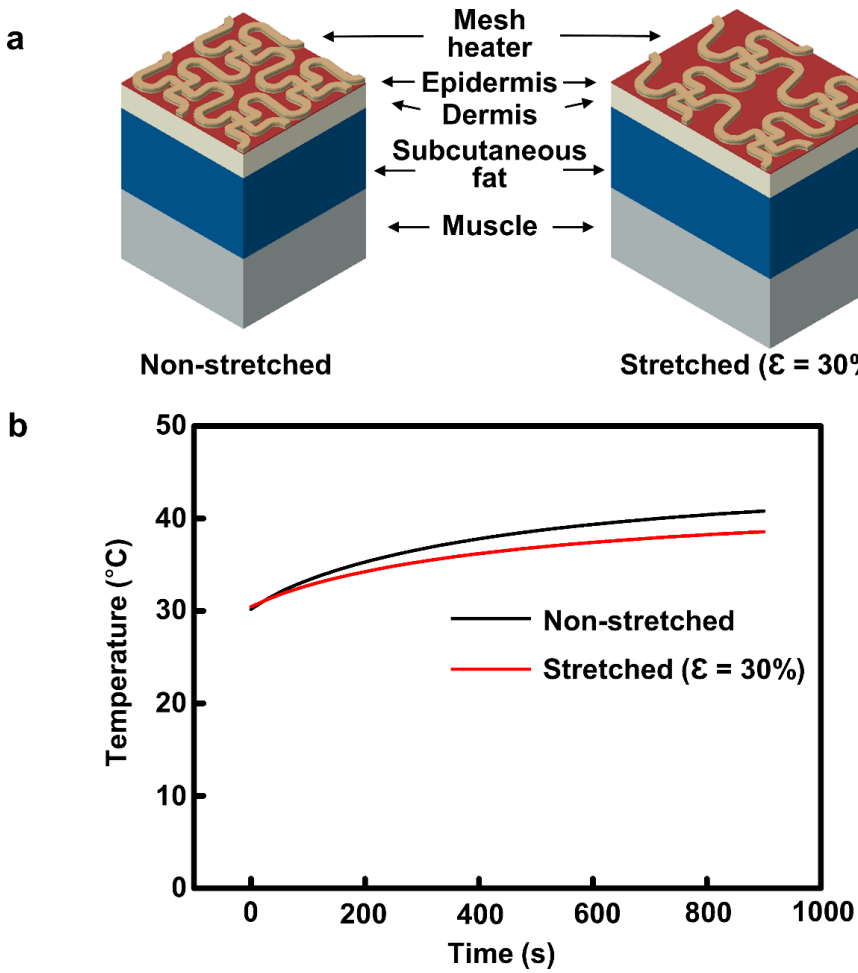

Figure 2.13 Computer simulation model and heat diffusion under stretching.

(a) Structure and composition of simulation model. (b) Simulation of the temperature profiles at the dermis. Heat transfer from the stretched mesh heater and the non-stretched mesh heater.

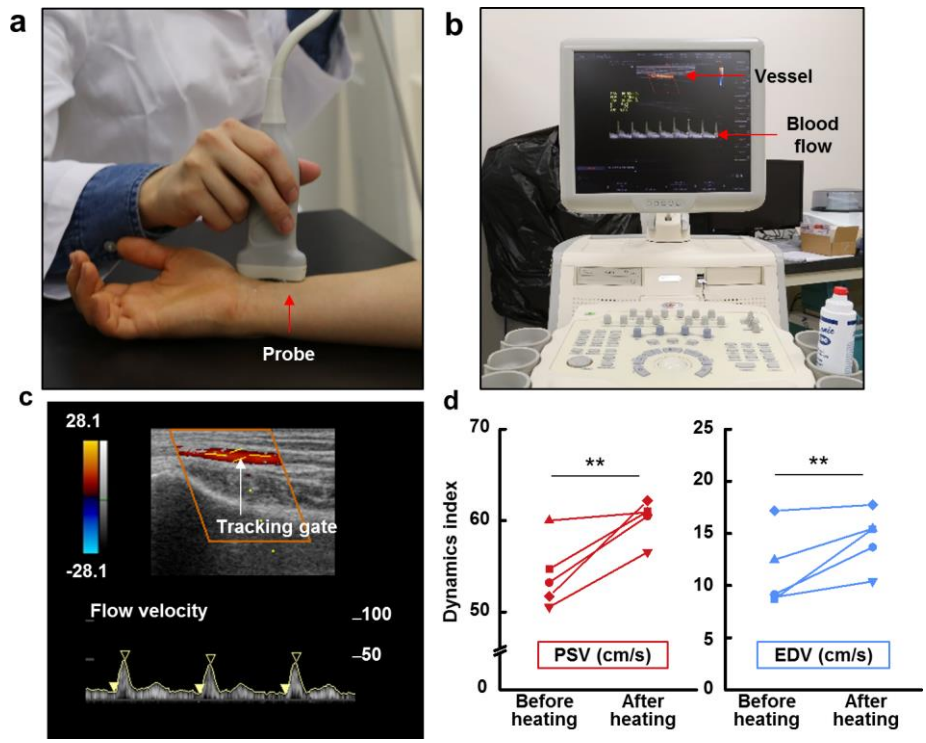

Figure 2.14 The physiologic effect of thermotherapy.

(a) Image showing the measurement with the ultrasound on the radial artery. (b) Photograph of the sonograph. The blood flow was measured by B-mode ultrasound. (c) A Doppler color image using B-mode ultrasound shows pulsatile blood flow in the radial artery located in the forearm. The blood-flow velocities were measured from a longitudinal duplex Doppler spectral waveform. (d) Comparison of peak systolic velocity (PSV) and end diastolic velocity (EDV) before and after heating (n = 5). ** $P < 0.05$ with a paired student t-test.

2.4 Conclusion

In summary, we demonstrate the fabrication and performance of the stretchable heater made of a homogeneous nanocomposite of Ag NWs and SBS elastomer. The high conductivity of the Ag NW/SBS nanocomposite runs the stretchable heater with low input voltages powered by a small battery. Furthermore, the mesh heater has a low system modulus and small changes in resistance under the uniaxial or biaxial strains. The heating profile on the wrist is uniform and stable despite large joint movements. This patterning process is also applicable to larger areas, which would allow the heater to cover knee or other body parts as well. Since the soft stretchable heater makes conformal contact with the skin, the heat transfer to muscles or blood vessels is effective. Integrating the stretchable heater with a custom-made electronic band provides further wearability and makes the system truly portable to perform the point-of-care articular thermotherapy.

2.5 Reference

(1) Coggon, D.; Croft, P.; Kellingray, S.; Barrett, D.; McLaren, M.; Cooper, C. Arthritis Rheum. **2000**, 43, 1443.

(2) Loeser, R. F.; Goldring, S. R.; Scanzello, C. R.; Goldring, M. B. Arthritis Rheum. **2012**, 64, 1697.

(3) Hartz, A. J.; Fischer, M. E.; Bril, G.; Kelber, S.; Rupley, D., Jr.; Oken, B.; Rimm, A. A. J. Chronic Dis. **1986**, 39, 311.

(4) Felson, D. T.; Naimark, A.; Anderson, J.; Kazis, L.; Castelli, W.; Meenan, R. F. Arthritis Rheum. **1987**, 30, 914.

(5) Maghsoudipour, M.; Moghimi, S.; Dehghaan, F.; Rahimpanah, A. J. Occup. Rehabil. **2008**, 18, 152.

(6) Lehmann, J. F. Therapeutic heat and cold; 4th ed.; Williams & Wilkins: Baltimore, **1990**.

(7) Brosseau, L.; Yonge, K. A.; Robinson, V.; Marchand, S.; Judd, M.; Wells, G.; Tugwell, P. Cochrane Database Syst Rev **2003**, CD004522.

(8) Petrofsky, J. S.; Laymon, M.; Lee, H. Med. Sci. Monit. **2013**, 19, 661.

(9) Michlovitz, S.; Hun, L.; Erasala, G. N.; Hengehold, D. A.; Weingand, K. W. Arch. Phys. Med. Rehabil. **2004**, 85, 1409.

(10) Webb, R. C.; Bonifas, A. P.; Behnaz, A.; Zhang, Y.; Yu, K. J.; Cheng,

H.; Shi, M.; Bian, Z.; Liu, Z.; Kim, Y. S.; Yeo, W. H.; Park, J. S.; Song, J.; Li, Y.; Huang, Y.; Gorbach, A. M.; Rogers, J. A. Nature materials **2013**, 12, 938.

(11) Son, D.; Lee, J.; Qiao, S.; Ghaffari, R.; Kim, J.; Lee, J. E.; Song, C.; Kim, S. J.; Lee, D. J.; Jun, S. W.; Yang, S.; Park, M.; Shin, J.; Do, K.; Lee, M.; Kang, K.; Hwang, C. S.; Lu, N.; Hyeon, T.; Kim, D. H. Nature nanotechnology **2014**, 9, 397.

(12) Kim, J.; Lee, M.; Shim, H. J.; Ghaffari, R.; Cho, H. R.; Son, D.; Jung, Y. H.; Soh, M.; Choi, C.; Jung, S.; Chu, K.; Jeon, D.; Lee, S. T.; Kim, J. H.; Choi, S. H.; Hyeon, T.; Kim, D. H. Nature communications **2014**, 5, 5747.

(13) Sekitani, T.; Noguchi, Y.; Hata, K.; Fukushima, T.; Aida, T.; Someya, T. Science **2008**, 321, 1468.

(14) Jung, S.; Kim, J. H.; Kim, J.; Choi, S.; Lee, J.; Park, I.; Hyeon, T.; Kim, D. H. Adv. Mater. **2014**, 26, 4825.

(15) Chun, K. Y.; Oh, Y.; Rho, J.; Ahn, J. H.; Kim, Y. J.; Choi, H. R.; Baik, S. Nature nanotechnology **2010**, 5, 853.

(16) Ma, R.; Lee, J.; Choi, D.; Moon, H.; Baik, S. Nano Lett. 2014, 14, 1944.

(17) Park, M.; Im, J.; Shin, M.; Min, Y.; Park, J.; Cho, H.; Park, S.; Shim, M. B.; Jeon, S.; Chung, D. Y.; Bae, J.; Park, J.; Jeong, U.; Kim, K. Nature nanotechnology **2012**, 7, 803.

(18) Moon, G. D.; Lim, G. H.; Song, J. H.; Shin, M.; Yu, T.; Lim, B.; Jeong, U. Adv. Mater. **2013**, 25, 2707.

(19) Kim, Y.; Zhu, J.; Yeom, B.; Di Prima, M.; Su, X.; Kim, J. G.; Yoo, S. J.; Uher, C.; Kotov, N. A. Nature **2013**, 500, 59.

(20) Lee, P.; Lee, J.; Lee, H.; Yeo, J.; Hong, S.; Nam, K. H.; Lee, D.; Lee, S. S.; Ko, S. H. Adv. Mater. **2012**, 24, 3326.

(21) Liang, J.; Li, L.; Niu, X.; Yu, Z.; Pei, Q. Nat. Photonics **2013**, 7, 817.

(22) Hu, L.; Kim, H. S.; Lee, J.-y.; Peumans, P.; Cui, Y. ACS nano **2010**, 4, 2955.

(23) Ge, J.; Yao, H. B.; Wang, X.; Ye, Y. D.; Wang, J. L.; Wu, Z. Y.; Liu, J. W.; Fan, F. J.; Gao, H. L.; Zhang, C. L.; Yu, S. H. Angew. Chem. Int. Ed. Engl. **2013**, 52, 1654.

(24) Lee, J.; Lee, I.; Kim, T. S.; Lee, J. Y. Small **2013**, 9, 2887.

(25) Korte, K. E.; Skrabalak, S. E.; Xia, Y. J. Mater. Chem. **2008**, 18, 437.

(26) Paul, A.; Zhen, Y. R.; Wang, Y.; Chang, W. S.; Xia, Y.; Nordlander, P.; Link, S. Nano Lett. **2014**, 14, 3628.

(27) Hsu, P. C.; Liu, X.; Liu, C.; Xie, X.; Lee, H. R.; Welch, A. J.; Zhao, T.; Cui, Y. Nano Lett. **2015**, 15, 365.

(28) Kim, T.; Kim, Y. W.; Lee, H. S.; Kim, H.; Yang, W. S.; Suh, K. S. Adv. Funct. Mater. **2013**, 23, 1250.

(29) Kennedy, J. E.; Higginbotham, C. L. In Biomedical Engineering,

Trends in Materials Science; InTech: **2011**.

(30) Dong, A.; Ye, X.; Chen, J.; Kang, Y.; Gordon, T.; Kikkawa, J. M.; Murray, C. B. J. Am. Chem. Soc. **2011**, 133, 998.

(31) Kim, D. H.; Lu, N.; Ma, R.; Kim, Y. S.; Kim, R. H.; Wang, S.; Wu, J.; Won, S. M.; Tao, H.; Islam, A.; Yu, K. J.; Kim, T. I.; Chowdhury, R.; Ying, M.; Xu, L.; Li, M.; Chung, H. J.; Keum, H.; McCormick, M.; Liu, P.; Zhang, Y. W.; Omenetto, F. G.; Huang, Y.; Coleman, T.; Rogers, J. A. Science **2011**, 333, 838.

(32) Xia, Y.; Whitesides, G. M. Annu. Rev. Mater. Sci. **1998**, 28, 153.

(33) Yousefpour, A.; Hojjati, M.; Immarigeon, J. P. J. Thermoplast. Compos. Mater. **2004**, 17, 303.

(34) Fan, J. A.; Yeo, W. H.; Su, Y.; Hattori, Y.; Lee, W.; Jung, S. Y.; Zhang, Y.; Liu, Z.; Cheng, H.; Falgout, L.; Bajema, M.; Coleman, T.; Gregoire, D.; Larsen, R. J.; Huang, Y.; Rogers, J. A. Nature communications **2014**, 5, 3266.

(35) Oosterveld, F. G.; Rasker, J. J. Semin. Arthritis Rheum. **1994**, 24, 82.

(36) Hattori, Y.; Falgout, L.; Lee, W.; Jung, S. Y.; Poon, E.; Lee, J. W.; Na, I.; Geisler, A.; Sadhwani, D.; Zhang, Y.; Su, Y.; Wang, X.; Liu, Z.; Xia, J.; Cheng, H.; Webb, R. C.; Bonifas, A. P.; Won, P.; Jeong, J. W.; Jang, K. I.; Song, Y. M.; Nardone, B.; Nodzenski, M.; Fan, J. A.; Huang, Y.; West, D. P.; Paller, A. S.; Alam, M.; Yeo, W. H.; Rogers, J. A. Adv Healthc Mater **2014**, 3, 1597.

(37) Lockhart, M. E.; Robbin, M. L.; Allon, M. J. Ultrasound Med. **2004**, 23, 161.

(38) Abramson Di, B. Y. T. S. J. M. R. C. G. Am. J. Phys. Med. **1960**, 39, 51.

Chapter 3. Electromechanical cardioplasty using a wrapped soft, highly conductive epicardial mesh

3.1 Introduction

Rapid conduction of electrical impluses make coordinated contraction of heart, pumping blood to whole body efficiently. Heart failure (HF) is often came from injuries of the specialized His-Purkinje conduction system[1]. Currently, patients undergo medical therapy in an attempt to reverse adverse mechanical remodeling. Biventricular pacing attempts to improve electrical dyssynchrony, but can only be applied to a subset of patients, and has a significant non-responder rate associated with it. Thus, a comprehensive approach to support the function of physiological system of diseased myocardium can be expected to open a new era of HF treatment.

Biventricular pacing, for which a subset of HF patients may qualify, has been proven to rapidly enhance cardiac function, alleviate symptoms, and improve long-term survival in numerous clinical trials.[2] This type of pacing improves inefficient pumping activity by reducing the dis-coordination of contractions in diseased hearts by pacing both chambers simultaneously. Therefore, it has been proposed as a standard therapy by the American College of Cardiology and the American Heart Association in the subset of patients who may benefit.[3] Despite these positive attributes, biventricular

pacing involves with the activation of the myocardium through electrical current sources originating from only two point electrodes located in dilated ventricle, rather than a more comprehensive approach where large areas of myocardium are activated simultaneously.

The concept of cardiomyoplasty, augmenting the function of diseased myocardium through a biventricular wrap, was introduced in the 1980's, and involved wrapping skeletal muscle (litissimus dorsi) around the heart to prevent post-myocardial infarction remodeling and to augment systolic function by pacing skeletal muscle flap.[4] Unfortunately, this initially attractive therapy faded from clinical practice because hemodynamic improvement in systolic function was not consistently demonstrated, and sudden death and arrhythmic events occurred during follow-up. Instead, a device encircling the heart or exogenous cardiac tissue patch implanted on the heart could act as a structural sub-component of myocardium to share myofiber stress (*29*), thereby contributing to a positive remodeling process and subsequent improvement of pumping activity. Human trials using devices wrapping the heart, such as the polyester mesh wrap (CorCap, Acorn Cardiovascular, Inc.) and the ventricular restraint nitinol mesh wrap (HeartNet, Paracor Medical Inc.) also showed controversial results. In a randomized clinical trial, the elastic mesh (HeartNet) wrapping the heart in patients with heart failure had no effect on functional end-points, particularly peak oxygen consumption, or survival.[5] The CorCap trial did

demonstrate significant improvement in prevention of ventricular remodeling, but controversial results in long-term survival[6,7]. Unlike these cardiac restraint devices that are relatively stiff and electrically non-conductive, we sough to fabricate highly conductive epicardium-like device with elastic properties nearly identical to epicardial tissue sheet.

Here, we introduce electromechanical cardioplasty using the epicardial mesh designed to mechanically integrate with the heart and act as a structural element of cardiac chambers. We also instilled the electrical function of a cardiac conduction system (His-bundles and Purkinje fiber network) into the mesh to deliver impulses to the whole ventricular myocardium in concert, rather than merely to small point electrodes in the ventricles. To achieve these, we explored candidate materials to be elastic and conductive as in cardiac tissue. Recently developed conductive and stretchable materials, such as gold-based composites[8,9] and carbon nanotube-based composites,[10,11] have shown potential as elasto-conductive materials. However, many technical issues, including low conductivity, poor elasticity, and/or high resistance change induced by strains, still remain. Meanwhile, silver nanowire (AgNW) networks are known to maintain high conductivity under repeatedly applied strains due to their mechanical deformability and highly percolated structures.[12,13] Styrene-butadiene-styrene (SBS) rubber, a biocompatible thermoplastic polymer, has high elasticity and reshaping capability because of its physically cross-linked

structure.[14,15] We chose AgNW and SBS rubber to fabricate the mesh-shaped substrate resembling elastic and electrical properties of cardiac tissue.

In post-infarct rats, the epicardial mesh integrated with the heart preserved diastolic relaxation, reduced inherent wall stress by sharing cardiac load as a structural component, improved cardiac contractile function through synchronized electrical stimulation, and terminated ventricular tachyarrythmia as an epicardial defibrillator. Our study demonstrates an improved therapeutic approach to electromechanical cardioplasty using an epicardial device that reconstructs the cardiac tissue form and its specialized functions.

3.2 Experimental Section

3.2.1 Study design

The aim of this study was to develop electromechanical cardioplasty by wrapping the epicardial surface of the heart in a mesh made of a nanocomposite of LE-AgNW/SBS. The device was designed to have an elastic modulus identical to that of the myocardium. Computer simulations estimated the effect of the epicardial mesh on cardiac hemodynamics. For in vivo experiments, rats were randomly assigned to control and myocardial infarction group. Treatment conditions were blinded during all experimental

processes. On the basis of our previous experiences with the post-myocardial infarction model, group sizes were determined; at least six rats were required to identify scar formation at 8 weeks after infarction since mortality is approximately 50% during an 8-week follow-up period. At eight-weeks after infarction, we evaluated the effect of electrical stimulation with the epicardial mesh device on total ventricular activation time, left ventricular function, myocardial wall stress, and LV pressure.

3.2.2 Fabrication of epicardial mesh

LE-AgNW/SBS (Kumho KTR-101, Kumho Petrochemical) solution was poured on the serpentine-shaped PDMS mold. The remaining solution on the top of the mold was removed with a blade. The molded solution was dried slowly at 45°C. The LE-AgNW/SBS solution was applied selectively on the bottom of PDMS mold to fabricate the electrodes which are contacted to the heart. Additional SBS solution was poured in the mold to encapsulate the LE-AgNW/SBS layer.

3.2.3 Histological analysis

Hearts were fixed in 10% formalin solution for 24 h at 4°C. Paraffin blocks were made, and 2- μm slides were prepared for Masson's trichrome staining, and 4-μm-thick tissue sections were prepared for macrophage assays. The sections were deparaffinized in xylene and hydrated by

immersing in a series of graded ethanol. Antigen retrieval was performed in a microwave by placing the sections in epitope retrieval solution (0.01 M citrate buffer, pH 6.0) for 20 minutes; endogenous peroxidase was inhibited by immersing the sections in 0.3% hydrogen peroxide for 10 minutes. Sections were then incubated with primary rabbit poly antibody to F4/80 (Santa Cruz) for macrophages. Staining for the detection of bound antibody was evaluated by DAB.

3.3 Result and Discussion

3.3.1 Soft, elastic, and highly conductive epicardial mesh design

The cardiac conduction system spreads across the endocardial surface of the ventricles and rapidly transfers electrical signals from endocardium to epicardium, by interfacing directly with cardiac muscles, to allow the heart to contract coordinately. For the elastic-conductive mesh device design, we tried to imitate that the heart in structural and functional aspect (Figure 3.1a). To give stable electrical conduction with elasticity, we made a stretchable conductive nanocomposite using ligand exchanged AgNW and SBS rubber. The high conductivity of LE-AgNW/SBS nanocomposite showed low impedance and high charge storage capacity due to the high electrical percolation network of AgNW. The electrical percolation network maintains the electrical conduction during systole and diastole cardiac cycle, which

enable electrical conduction form heart to nanocomposite for recording continuously and from nanocomposite to heart for stimulating the heart to pump (Figure 3.1b).

Next, we optimized the mechanical properties of the LE-AgNW/SBS nanocomposite. Encircling the heart with a high modulus film may reduce diastolic compliance, thereby aggravating heart failure symptoms.[16] Therefore, we attempted to design a device which has comparable mechanical properties to that of the rat myocardium, to conform anatomically to epicardial surface with conformal contact. To tailor mechanical elasticity of the LE-AgNW/SBS nanocomposite, a mesh design was applied using a polydimethylsiloxane (PDMS) mold (Figure. 3.1c). The double layer structure of LE-AgNW/SBS nanocomposite and an SBS rubber layer enhanced durability and elasticity. The elastic modulus was 44.71 ± 7.54 kPa in serpentine mesh and 3.39 ± 0.849 kPa in hyperserpentine mesh, depending on the extent of curvature of the serpentine structure. The serpentine and hyperserpentine meshes exhibited remarkably softer mechanical properties than the film of the same material (Figure. 3.1e).

We then resected epicardial tissue sheets from rat hearts and measured the modulus of epicardial tissue sheets, which was 34.67 ± 6.2 kPa (n = 3). The circumferential strain (change of circumference between end-diastole and end-systole divided by circumference at end-diastole) of epicardium estimated by echocardiography, was 14.1 as 14% in control hearts (n = 4)

and 4.6 n = 4% in 8-week post-myocardial infarction (post-MI) rat hearts (n = 3) (Figure. 3.1f). From these results, a serpentine mesh design was selected because its elasticity is comparable to that of epicardium within 20% of physiological strain in cardiac movement. The epicardial mesh showed stable electrical resistance under applied strains. The electrical property was consistent with only 1.02-fold increase over 10,000 repetitive stretching cycles, approximating 3 hours of cardiac movement in humans.

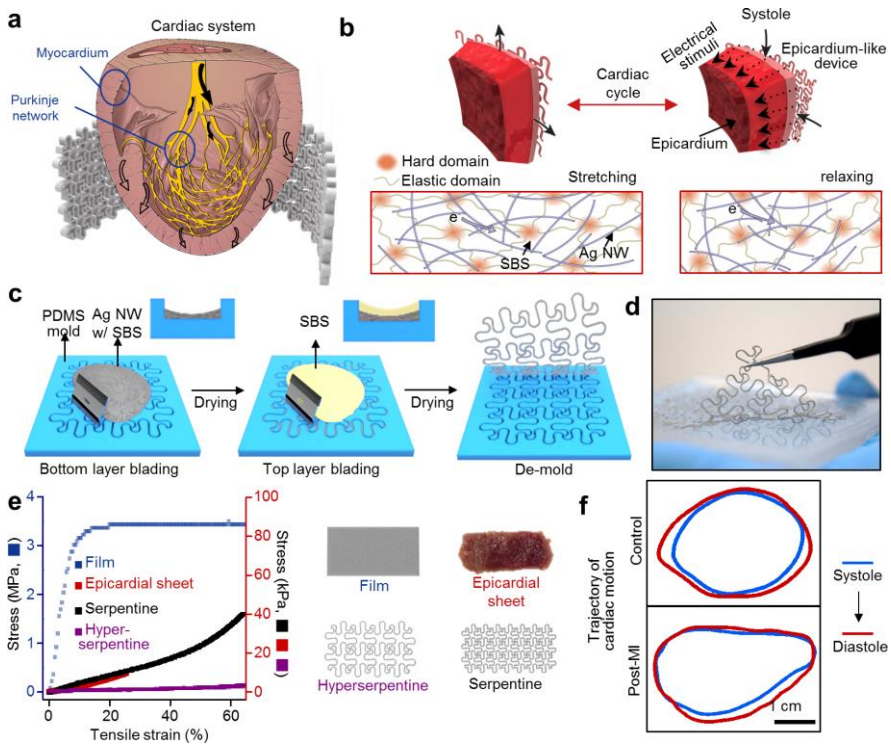

Figure 3.1 Strategy of materials and design for epicardial mesh.

(a) Schematic illustration of the design strategy of an epicardial mesh for electromechanical cardioplasty in accordance with electrophysiological conduction in the cardiac system. (b) Conductive nanowires were homogeneously dispersed in SBS rubber, allowing for electrical signal (e−) transfer during the entire cardiac cycle. (c) Schematic illustration of the epicardial mesh fabrication. (d) A photograph of demolding mesh from PDMS mold (e) Average stress-strain curves measure from left panel of samples (epicardial sheet, serpentine mesh, hyperserpentine mesh, and film). (f) Trajectory of moving control rat heart and post-MI rat heart at end systole (blue) and end diastole (red).

3.3.2 Personalization of epicardial mesh

Figure 3.2a showed a designed epicardial mesh. The size of the electrodes could cover the whole ventricles [right ventricle (RV), 12.5 × 10 mm; left ventricle (LV), 17 × 10 mm; thickness, 100 μm]. This design enabled the current flow by electrical stimulation to be broadly distributed, allowing rapid propagation of depolarization of the myocardium as shown in the previous reports.[17,18] The device was composed of two wide electrodes, which were positioned on the RV and the LV, with an insulating section between the each electrodes and supporting sections at the ends to support wrapping he heart with entire epicardial mesh. The mass of silver was about 20 mg/device.

The outside of the epicardial mesh was coated with an SBS to insulate the electrodes (Figure 3.2b). The device elasticsity was confirmed by pulling (L0 = 60 mm to L1 = 90 mm) and releasing the mesh (L1 to L0`= 60 mm) (Figure. 3.2c). Using a 3D image created by cardiac computed tomography (CT) (Figure 3.2d and 3.2e), we could make an anatomically personalized design for the rodents. The final design was confirmed by wrapping a 3D-printed heart model with the mesh tailored to the rat's cardiac parameters, including the size of each sections (RV, LV, I, and S) and the overall size measured at systole (Figure 3.2f).

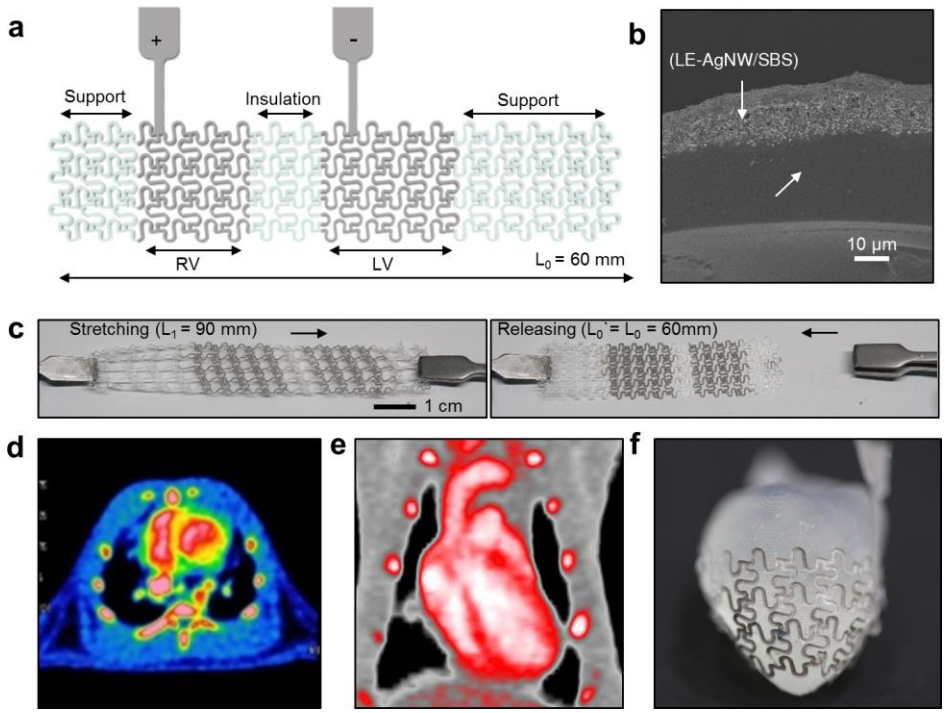

Figure 3.2 Fabrication of elastic epicardial mesh.

(a) An illustration of the epicardial mesh, indicating the individual sections. (b) A SEM image of cross-sectional of an electrode in epicardial mesh. (c) Manual stretching and releasing test of epicardial mesh. (d) A cardiac CT image in axial plane. (e) Longitudinal image of cardiac CT. (f) An epicardial mesh wrapped the 3D printed heart model.

3.3.3 The mechanical effect of the epicardial mesh is estimated by computer simulation

We estimated the mechanical effects of the epicardial mesh on rat heart diastolic function through a biventricular finite element (FE) model constructed from high-resolution CT images, with continuous transmural fiber orientations across its thickness (Figure 3.3a). Diastolic expansions of three cases on the wrapping model (Figure 3.3b) were compared: i) without any wrap on the heart; ii) with the wrap using epicardial mesh (E = 50 kPa); and iii) with the wrap of unpatterned device (continuous thin film; E = 47 MPa). The effects of the epicardial mesh or film wrap on end-diastolic pressure-volume relationship (EDPVR) were analyzed (Figure 3.3c). Compared to the control (no wrapping), the film wrap constrained heart inflation and elevated end-diastolic pressure, possibly leading to increased backward pressure to the left atrium and pulmonary vascular congestion. In contrast, the epicardial mesh wrap did not show any appreciable effect. Notably, the film of LE-AgNW/SBS nanocomposite caused diastolic collapse in the RV in silico (Figure 3.3d), implying a significant risk of hemodynamic instability. In contrast, the epicardial mesh wrap did not affect the shape or curvature of ventricular chambers during the simulated cardiac cycle.

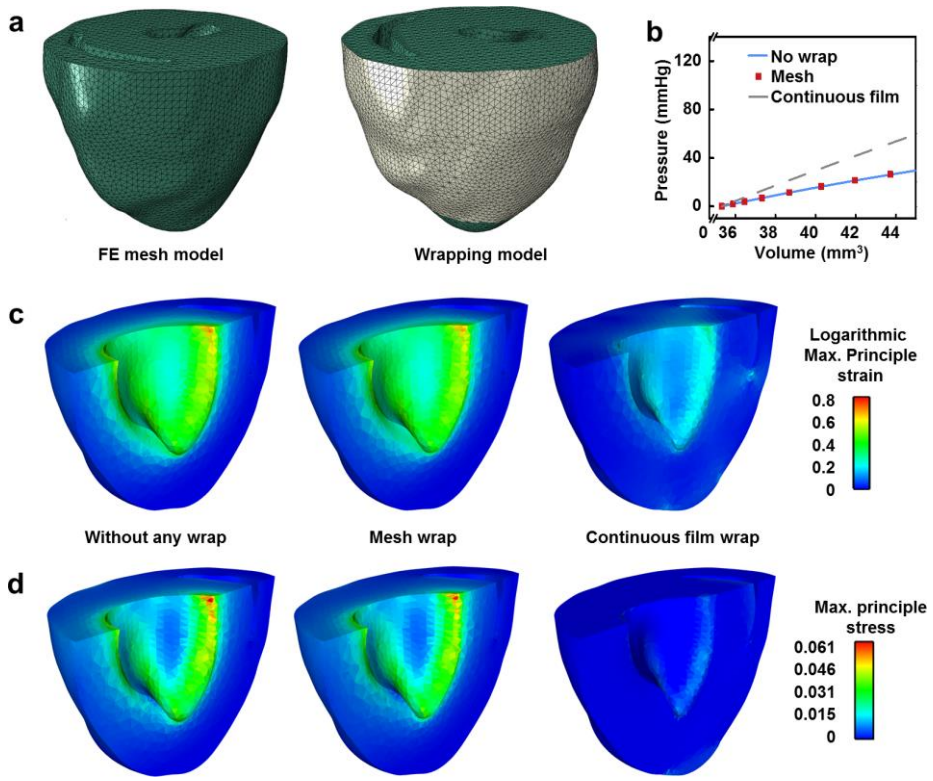

Figure 3.3 Computer simulation for effects of epicardial mesh.

(a) The biventricular finite element model mesh model (left panel). Gray shell elements (right panel) represent the device wrap. The apex was not covered by the wrap. (b) Influences of various wraps on left ventricular end-diastolic pressure-volume relationship (EDPVR). (c) Logarithmic maximum principal strain distribution without sock, with the mesh wrap, and with the continuous film wrap.

3.3.4 The epicardial mesh integrates with the moving rat heart, without impeding diastolic relaxation

We tested conformal contacts of epicardial mesh on the moving heart and consistently monitored electrical activities of heart in vivo. A custom-designed epicardial mesh was implanted in a control rat (Figure 3.4a). Baseline surface ECG, conventional bipolar electrode, and epicardial mesh simultaneously detected cardiac electrical activity (Figure 3.4b). Phase consistency of the whole electrograms and the severity of the baseline drift were compared between a conventional bipolar electrode and an epicardial mesh. After ubtracting QRS-T complexes, average absolute deviation of the baseline drift was significantly less with the epicardial mesh than the conventional electrode (Figure. 3.4d), suggesting the conformal contact of the epicardial mesh on the moving heart.

Next, we tested that the elastic epicardial mesh that impacts on diastolic relaxation and wall stress of myocardium. The epicardial mesh was desired to be shared the stress of myocardium, which resulted in by reducing stress of the host-myocardium, but not disturbing diastolic relaxation.

The effect of the epicardial mesh on diastolic function was evaluated at baseline and during right atrial pacing (RAP) and mesh pacing (MeshP) at the same cycle length of 420, 300, and 280 ms in control (n = 5) and 8-week post-MI rats (n = 5), since diastolic relaxation is influenced by heart rate. The implanted epicardial mesh did not considerably shift the left ventricular

end-diastolic pressure (LVEDP), and (tau), which corresponding ot index of compliance and diastolic relaxation respectively, at baseline (sinus rhythm) and under electrical stimulation (Figure. 3.5a and 3.5b; all $P > 0.05$ by linear mixed model).

We tried to study the effect of the epicardial mesh on reducing myocardial stress.[19] While the electrical stimulation was occurred by the epicardial mesh, longitudinal wall stress was reduced during diastole and systole in the post-MI heart and somewhat reduced in the control rat heart (Figure 3.5c).

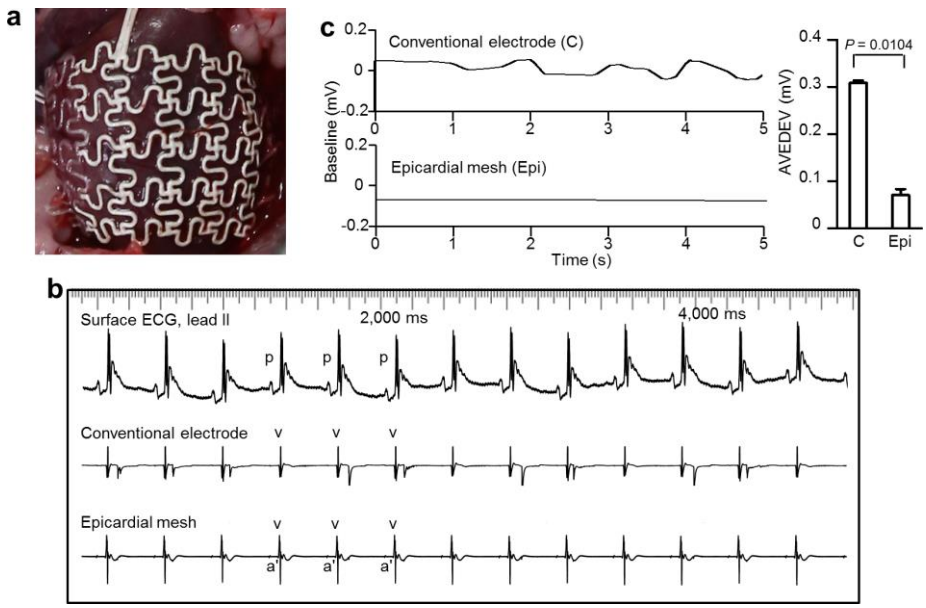

Figure 3.4 Coupling effect of the epicardial mesh to the rat heart.

(a) Implantation of epicradial mesh in a control rat heart. (b) Surface ECG (lead II) and intracardiac electrograms recorded from a conventional electrode on the RV and the epicardial mesh encircling the heart. p, p-wave; v, ventricle; a′, atrium. (c) From intracardiac electrograms of the conventional electrode (C) and epicardial mesh (Epi), the baselines are extracted using peak analysis software. Average absolute deviation (AVEDEV) was calculated from the baseline. Data are averages ± SEM (n = 3). P value was determined by unpaired Student's t test.

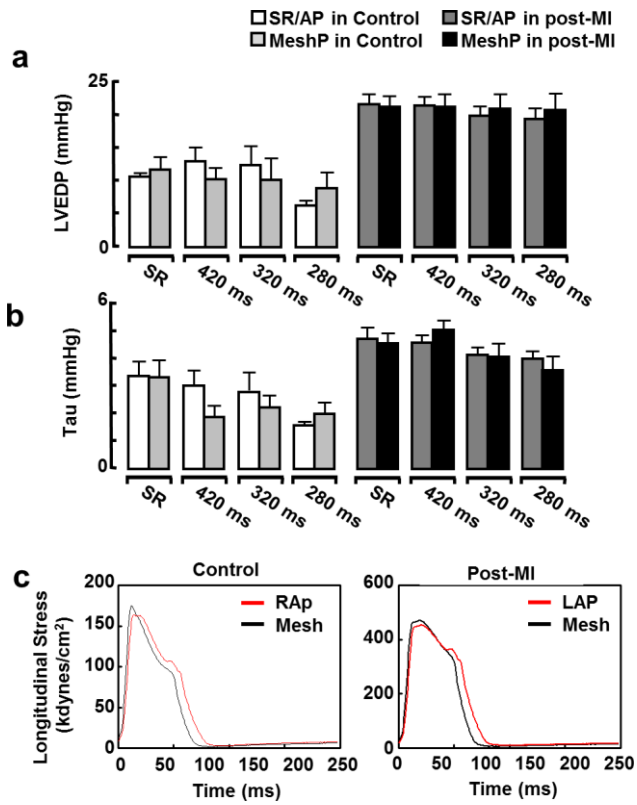

Figure 3.5 Hemodynamic and structural effects of electromechanical cardioplasty.

(a) Effect of the epicardial mesh on LVEDP in control and 8-week post-MI rats. (b) Effect of the epicardial mesh on tau in control and 8-week post-MI rats. (c) LV wall stress-pressure loop in control rat herat and post-MI rat heart during one cardiac cycle.

3.3.5 Electrical stimulation restores total ventricular activation time and improves systolic function

We studied whether epicardial mesh could activate heart synchronously with electrical stimulation, shortening QRS duration. The average QRS duration at baseline in 8-week post-MI rats was fairly more dragged out than in controls, (meaning injuries of myocardium and/or the conduction system because of heart disease. Globalized pacing was then continuously delivered with 280 ms of cycle length through the epicardial mesh post-MI rats (Figure 3.6a). In controls, QRS duration during epicardial mesh pacing was nearly identical to that of in baseline (Figure 3.6b and 3.6c).

All post-MI rats that completed the electrophysiology study showed the effective normalization of QRS duration (≤ 27 ms) by epicardial mesh pacing, except for one animal where QRS duration was reduced from 66 ms to 37 ms. To evaluate the possibility that QRS duration varied with heart rate, we measured the QRS duration at multiple heart rates in all rats. We found that heart rates were unrelated to QRS duration (Figure 3.7a). We also found that epicardial mesh pacing at 90% of the baseline cycle length (10% faster than the native heart rate) shortened the QRS duration compared to the non-paced, native QRS duration at baseline (Figure 3.7b) but this was tested only in 2 of the animals from Fig. 6B (that had the cycle length of MeshP similar to that of baseline) and would need further exploration. These data suggest that electrical stimulation therapy with the epicardial

mesh in an 8-week post-MI heart restores overall electrical activation time of the ventricles to near-normal activation time.

We further confirmed the enhancement of cardiac functions by pacing with the epicardial mesh. In 2-D echocardiography, post-MI rats showed enlarged LV end-systolic diameter (LVESD) compared to the controls at baseline (Figure 3.8a and 3.9).

To explore how pacing through epicardial mesh leads to overall recovery of cardiac pumping functions, we measured peak radial strain from each segments of the LV wall In post-MI rats, weakened strains of individual LV segment were considerably enhanced by pacing with 280 ms Cycle length (Figure 3.8c and 3.10). Contractility (dP/dtmax) was also more increased by the epicardial mesh pacing than RAP (Figure 3.8d and 3.11).

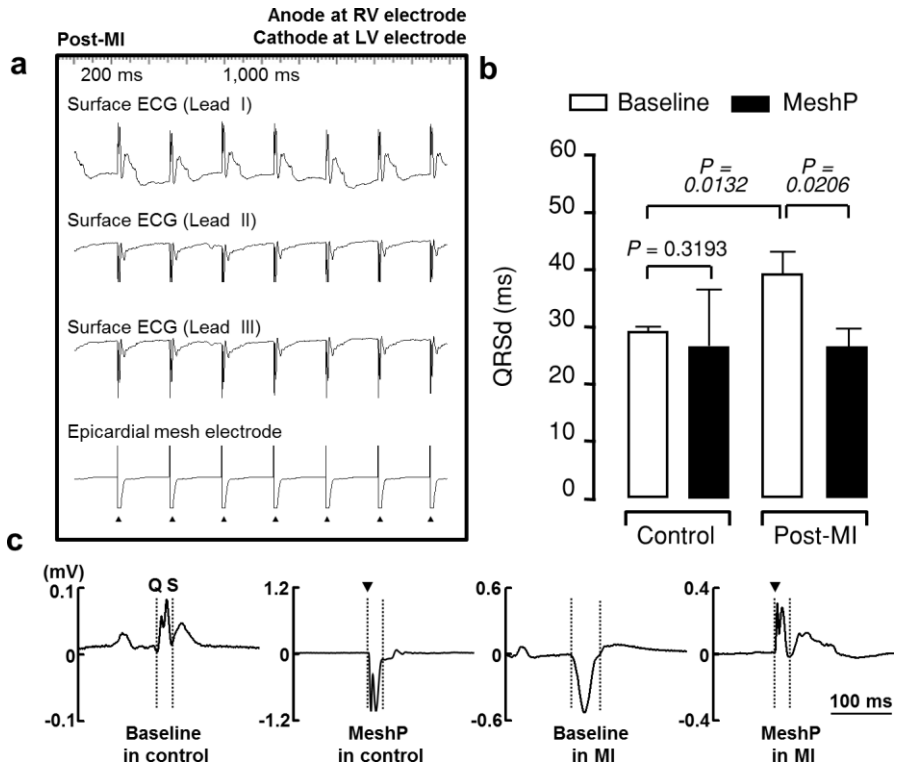

Figure 3.6 Comparision of QRS duration.

(a) Surface ECG strips (lead I, II, and III) are recorded during electrical stimulation by the epicardial mesh in post-MI rat. (b) The effect of pacing through the epicardial mesh on QRS durations in 9 control rats and 12 post-MI rats. (unpaired student *t*-tests, $*P < 0.05$.)

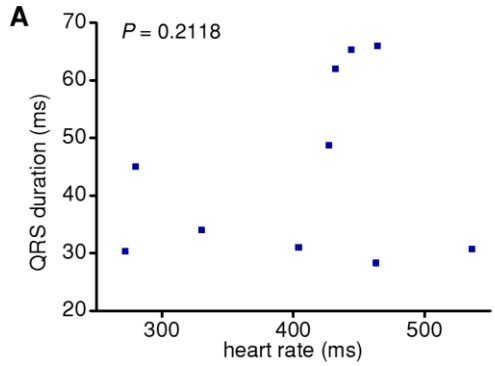

B

No	Baseline		Mesh pacing at cycle lengths of 280ms	
	heart rate (ms)	QRS duration (ms)	Percentage pacing cycle lengths	QRS duration (ms)
Post-MI Rat #1.	280	45	90%	26
Post-MI Rat #2.	272	30.3	90%	21

Figure 3.7 The relation of heart rates to QRS durations, and epicardial mesh pacing at 90% of the baseline cycle lengths.

(a) The correlation of heart rates and QRS duration at baseline. Data are individual post-MI rats (n = 10). P value determined by the Pearson correlation test. (b) The effect of pacing at 90% of baseline cycle lengths on QRS duration. Data are for n = 2 post-MI animals from (A), before and after pacing at 90%. The animals were chosen because their baseline heart rates were similar.

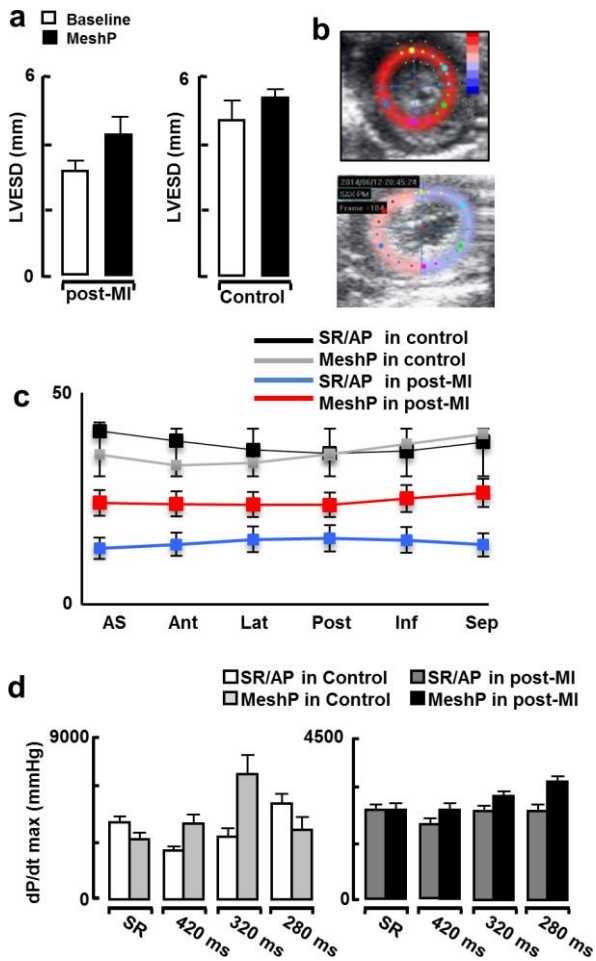

Figure 3.8 The effect of electrical stimulation on cardiac electrical and mechanical function.

(a) LVESD changes after electrical stimulation through epicardial mesh in control rats and post-MI rats. (b) A speckle tracking radial strain image indicates the color coded 2D mode at baseline (sinus rhythm). (c) Speckle tracking of radial strain in control (n = 5) and 8-week post-MI hearts (n = 6). (d) dP/dt_{max} which is LV contractility index during RAP and MeshP in control (n = 5) and 8-week post-MI rats (n=5)

Group	Rat #.	Baseline			MeshP		
		LVEDD (mm)	LVESD (mm)	FS (%)	LVEDD (mm)	LVESD (mm)	FS (%
Control	1	0.7	0.33	52.86	0.54	0.26	51.8
	2	0.53	0.25	52.83	0.52	0.21	59.6
	3	0.52	0.26	50.00	0.54	0.24	55.5
	4	0.68	0.32	52.94	0.5	0.21	58.0
Post-MI	5	0.47	0.39	17.02	0.44	0.32	27.2
	6	0.48	0.37	22.92	0.4	0.27	32.5
	7	0.62	0.48	22.58	0.44	0.3	31.8
	8	0.88	0.66	25.00	0.77	0.54	29.8
	9	0.6	0.45	25.00	0.45	0.27	40.0

Figure 3.9 Echocardiographic data LVEDD, LVESD, and FS in control and 8-week post-MI rats.

MeshP, epicardial mesh pacing; LVEDD, left ventricular end-diastolic dimension; LVESD, left ventricular end-systolic dimension; FS, percentage fractional shortening

Group	Rat #	Baseline					
		AS (%)	Ant (%)	Lat (%)	Post (%)	Inf (%)	Sep (%)
Control	1	42.65	45.7	52.6	44.08	47.12	50.33
	2	31.95	32.97	33.57	30.4	29.27	31.92
	3	28.59	28.2	26.35	27.81	26.34	25.05
	4	43.05	47.57	54.75	42.22	44.74	50.91
	5	30.79	32.78	35.55	30.44	31.57	34.15
Post-MI	6	7.69	6.41	8.37	7.46	8.77	10.12
	7	15.31	15.36	16.4	15.82	16.53	17.31
	8	9.54	8.22	5.77	12.55	12.75	6.98
	9	15.21	10.54	2.19	12.33	5.81	1.42
	10	20.4	16.96	15.77	16.78	18.99	21.45
	11	14.51	13.03	8.68	13.32	9.85	6.01
Group	Rat #	MeshP					
		AS (%)	Ant (%)	Lat (%)	Post (%)	Inf (%)	Sep (%)
Control	1	35.87	32.1	34.2	39.08	38.5	38.21
	2	28.19	28.41	30	30.66	34.61	37.12
	3	28.3	30.32	34.13	28.99	32.83	37.87
	4	34.23	32.93	32.37	36.05	37.17	34.36
	5	64.67	64	43.84	52.68	43.26	39.83
Post-MI	6	12.22	12.5	17.96	15.81	22.42	28.07
	7	23.8	26.26	28	22.4	22.62	24.88
	8	12.99	12.87	14.2	13.81	14.74	15.58
	9	21.55	21.01	14.3	16.21	8.3	7.12
	10	-	-	-	-	-	-
	11	27.23	33.5	38.98	22.95	22.91	30.75

Figure 3.10 Speckle tracking radial strain data in control and 8-week post-MI hearts.

#10 post-MI rat died due to arrhythmic event prior to epicardial mesh pacing (MeshP). AS, anteroseptal; Ant, anterior; Lat, laterial; Post, posterior; Inf, inferior; Sep, septal.

Group	Rat #	dP/dt_{max} (mmHg/ms)	
		RAP	MeshP
Control	1	3840	3355
	2	3159	5631
	3	3503	2795
	4	4838	6179
	5	1902	1057
Post-MI	6	1386	1667
	7	3087	2949
	8	1542	2031
	9	3523	4016
	10	2278	2783

Figure 3.11 LV contractility index, dP/dtmax, during right atrial pacing (RAP) and MeshP in controls and 8-week post-MI rats.

RAP, right atrial pacing; MeshP, epicardial mesh pacing

3.3.6 Biocompatibility of the epicardial mesh and alternative gold-passivated mesh

Prior to translation, we tested the cellular toxicity and inflammatory reaction of the LE-AgNW/SBS. The mesh made of LE-AgNW/SBS (63:35 ratio) was then implanted in one rat heart and in the skeletal muscles of three rats (abdominal rectus muscle in two rats and femoral muscle in one rat; Figure 3.12a and 3.12b). Histology 3 weeks after implant revealed relatively minimal inflammatory infiltrates (Figure 3.12c).

We also looked into gold-coated LE-AgNW/SBS meshes that might be more desirable in humans, owing to inherent inert properties.[20] Therefore, we passivated the surface of LE-AgNW/SBS with a gold thin film deposited by thermal evaporation (Figure 3.13a). Inductively coupled plasma mass spectrometry (ICP-MS) analysis showed that silver ions did not leach out from the gold-coated mesh, but not more so than the regular mesh (Figure. 3.13b). H&E staining and macrophage assay of a rat skeletal muscle also revealed less inflammatory infiltrate in the Au-coated LE-AgNW/SBS mesh (Figure 3.13c). Furthermore, the electrical properties of the Au-coated LE-AgNW/SBS mesh were the same as those of the LE-AgNW/SBS mesh under mechanical deformation, thus, the Au-coated LE-AgNW/SBS mesh exhibited clear cardiac electrical activity in a control rat *in vivo*.

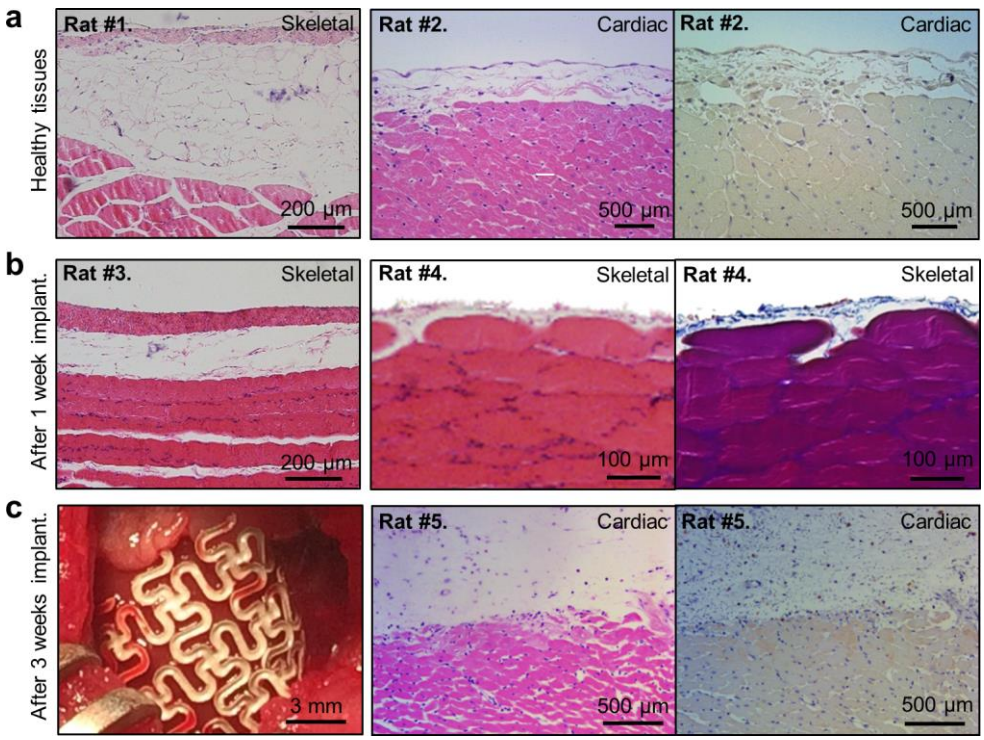

Figure 3.12 Histological analysis for biocompatibility test of epicardial mesh.

(a) Representative H&E stains (left and middle panels) and macrophage assay (F4/80, right) from healthy rodent skeletal and cardiac tissues without epicardial mesh implantation. (b) Epicardial meshes composed of LE-AgNW/SBS (65:35) implanted in the skeletal muscle for one week. Representative H&E stain (left and middle panels) and Masson's trichrome histology (right panel). (c) H&E stain (middle panel) and macrophage assay (F4/80, right) from one rat heart (left) where an epicardial mesh was implanted for 3 weeks

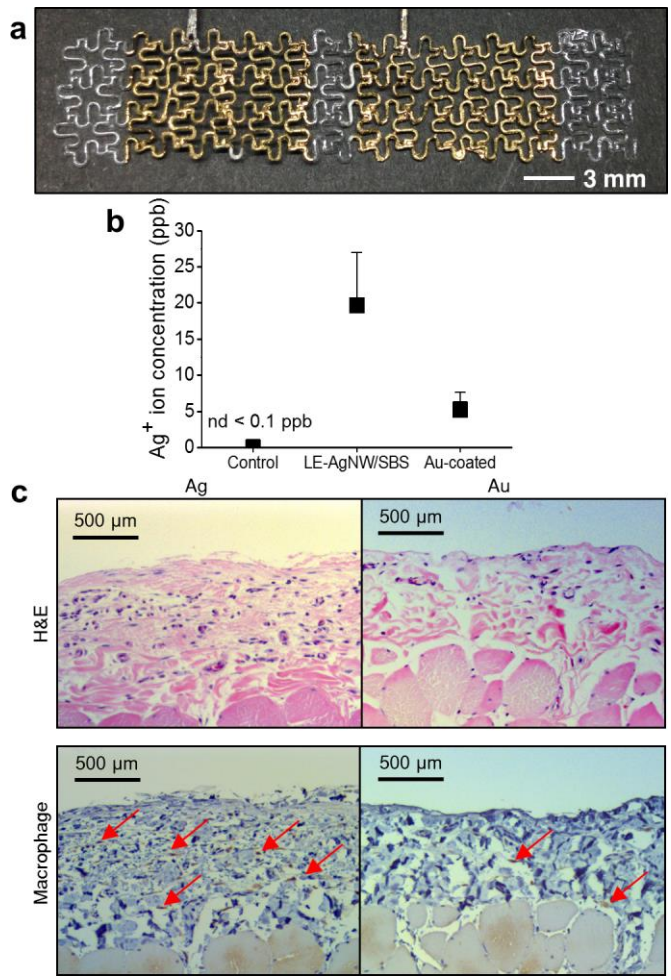

Figure 3.13 Biocompatibility of the gold coated device.

(a) Gold-deposited on the electrodes of the epicardial mesh. (b) Silver ion concentration was measured by ICP-MS analysis. Data are means ± SEM (*n* = 3). (c) Comparison of the H & E staining and immunohistochemistry for macrophage after implantation of epicardial mesh with and without Au-coated.

3.4 Conclusion

Heart failure can be treated by electrical stimulation to keep the beats in rhythm, but conventional electrical stimulation method through catheter electrode apply the electrical stimulation at specific points which causes low portion of patients who can have benefits from cardiac resynchronized therapy. To overcome the limitation, we fabricated epicardial mesh that wraps around the heart to deliver impulses to the whole ventricular myocardium. In post-MI rats, the epicardial mesh integrated structurally and electrically with myocardium and exerted beneficial effects, including preserved diastolic relaxation, reduced wall stress, and improved cardiac contractility. The improvement of biocompatibility through gold-coated epicardial mesh would provide further possibility to be an actual clinical application.

3.5 Reference

(1) Josephson, M. E. *Clinical Cardiac Electrophysiology: Techniques and Interpretations*; Wolters Kluwer Health/Lippincott Williams & Wilkins, 2008.

(2) Tang, A. S. L.; Wells, G. A.; Talajic, M.; Arnold, M. O.; Sheldon, R.; Connolly, S.; Hohnloser, S. H.; Nichol, G.; Birnie, D. H.; Sapp, J. L.; Yee, R.; Healey, J. S.; Rouleau, J. L. *N. Engl. J. Med.* **2010**, *363*, 2385.

(3) Writing Committee, M.; Yancy, C. W.; Jessup, M.; Bozkurt, B.; Butler, J.; Casey, D. E., Jr.; Drazner, M. H.; Fonarow, G. C.; Geraci, S. A.; Horwich, T.; Januzzi, J. L.; Johnson, M. R.; Kasper, E. K.; Levy, W. C.; Masoudi, F. A.; McBride, P. E.; McMurray, J. J.; Mitchell, J. E.; Peterson, P. N.; Riegel, B.; Sam, F.; Stevenson, L. W.; Tang, W. H.; Tsai, E. J.; Wilkoff, B. L.; American College of Cardiology Foundation/American Heart Association Task Force on Practice, G. *Circulation* **2013**, *128*, e240.

(4) el Oakley, R. M.; Jarvis, J. C. *Circulation* **1994**, *90*, 2085.

(5) Costanzo, M. R.; Ivanhoe, R. J.; Kao, A.; Anand, I. S.; Bank, A.; Boehmer, J.; Demarco, T.; Hergert, C. M.; Holcomb, R. G.; Maybaum, S.; Sun, B.; Vassiliades, T. A., Jr.; Rayburn, B. K.; Abraham, W. T. *J. Card. Fail.* **2012**, *18*, 446.

(6) Mann, D. L.; Kubo, S. H.; Sabbah, H. N.; Starling, R. C.; Jessup, M.; Oh,

J. K.; Acker, M. a. *J. Thorac. Cardiovasc. Surg.* **2012**, *143*, 1036.

(7) Rubino, A. S.; Onorati, F.; Santarpino, G.; Pasceri, E.; Santarpia, G.; Cristodoro, L.; Serraino, G. F.; Renzulli, A. *Ann. Thorac. Surg.* **2009**, *88*, 719.

(8) Moon, G. D.; Lim, G. H.; Song, J. H.; Shin, M.; Yu, T.; Lim, B.; Jeong, U. *Adv. Mater.* **2013**, *25*, 2707.

(9) Xu, L.; Gutbrod, S. R.; Bonifas, A. P.; Su, Y.; Sulkin, M. S.; Lu, N.; Chung, H. J.; Jang, K. I.; Liu, Z.; Ying, M.; Lu, C.; Webb, R. C.; Kim, J. S.; Laughner, J. I.; Cheng, H.; Liu, Y.; Ameen, A.; Jeong, J. W.; Kim, G. T.; Huang, Y.; Efimov, I. R.; Rogers, J. A. *Nat Commun* **2014**, *5*, 3329.

(10) Chun, K. Y.; Oh, Y.; Rho, J.; Ahn, J. H.; Kim, Y. J.; Choi, H. R.; Baik, S. *Nat. Nanotechnol.* **2010**, *5*, 853.

(11) Sekitani, T.; Noguchi, Y.; Hata, K.; Fukushima, T.; Aida, T.; Someya, T. *Science* **2008**, *321*, 1468.

(12) Hu, L.; Kim, H. S.; Lee, J. Y.; Peumans, P.; Cui, Y. *ACS Nano* **2010**, *4*, 2955.

(13) Lee, P.; Lee, J.; Lee, H.; Yeo, J.; Hong, S.; Nam, K. H.; Lee, D.; Lee, S. S.; Ko, S. H. *Adv. Mater.* **2012**, *24*, 3326.

(14) Yang, J. M.; Tsai, S. C. *Mater. Sci. Eng. C* **2010**, *30*, 1151.

(15) Kennedy, J. E.; Higginbotham, C. L. In *Biomedical Engineering, Trends in Materials Science*; InTech: 2011.

(16) Mann, D. L. *Braunwald's Heart Disease: A Textbook of Cardiovascular*

Medicine, 2-volume Set; Saunders (W B) Company Limited, 2014.

(17) Faria, P.; Hallett, M.; Miranda, P. C. *J Neural Eng* **2011**, *8*, 066017.

(18) Stevens-Lapsley, J. E.; Balter, J. E.; Wolfe, P.; Eckhoff, D. G.; Schwartz, R. S.; Schenkman, M.; Kohrt, W. M. *Phys. Ther.* **2012**, *92*, 1187.

(19) Opie, L. H. *Heart Physiology: From Cell to Circulation*; Lippincott Williams & Wilkins, 2004.

(20) Sperling, R. A.; Rivera Gil, P.; Zhang, F.; Zanella, M.; Parak, W. J. *Chem. Soc. Rev.* **2008**, *37*, 1896.

* From [Park, J.; Choi, S.; Janardhan, A. H.; Lee, S.; Raut, S.; Soares, J.; Shin, K.; Yang, S.; Lee, C.; Kang, K.; Cho, H. R.; Kim, S. J.; Seo, P.; Hyun, W.; Jung, S.; Lee, H.; Lee, N.; Choi, S. H.; Sacks, M.; Lu, N.; Josephson, M. E. **2016**, *8* (344), entitled, "Electromechanical cardioplasty using a wrapped elasto-conductive epicardial mesh"]. Reprinted with permission from AAAS.

Chapter 4. Highly conductive and biocompatible stretchable conductor for 3D multi-polar cardiac sock

4.1 Introduction

Heart is one of the most important organ that is activated by propagation of electrical conduction through the His-Purkinje conduction system. Monitoring electrical activities of cardiac helps the doctor to give an insight into the heart condition to diagnosis specific diseases, which is determined by a waveform of action potential in clinical care. In particular, local activation maps provide information of the location of the impaired myocardium, thus, multiple spatially distributed recordings are demanded for interpreting comprehensive heart diseases. However, the current generation of clinical Ag@Au core shell electro-anatomic mapping system using catheter electrodes does not support the real-time construction of electrical activity, necessitating off-line custom analysis[1]. In order to overcome asynchronous measurement of activation map, a nylon woven sock-mesh accompanied with button type electrodes was developed[2,3]. However, the electrodes were too big and stiff to provide proper contact to the epicardial surface, which can lead to a poor signal quality. Also the lack of elasticity of the sock-mesh may occur disturbing diastolic relaxation, leading other side effects. In diseased myocardium, once the cardiac muscle

was impaired, the response to pacing vary from pacing site to site. The conventional anatomical approach of the catheter electrode through the blood vessels makes electrical pacing at the desired site of the heart difficult. Therefore, new pacing attempt based on the impaired region monitoring is required to improve systolic function.

Recent achievement of stretchable electronic devices lead the development of ex vivo soft heart sock membrane that integrated with multifunctional sensor arrays[4]. The various sensors fabricated by photolithography measured changes in various condition of the heart during cardiac pumping cycle by conformal contact to the heart, yet, the processed materials are intrinsically brittle and expensive. Thereby, alternative stretchable conducting materials were craved to be developed to be closer to actual clinical practice.

Here, we introduce intrinsically stretchable and highly conductive rubber composed of gold shell silver nanowire and poly styrene-butadien-styrene rubber. Although gold nanowire has been developed with various synthesis methods[5,6], the conductivity and mechanical properties are still insufficient to utilize as a conductive nanocomposite due to its very small diameter (~100 nm) and long chain of ligand. However, silver nanowires (AgNW) are well known nanomaterial as a high conductive material with high aspect ratio, thus, AgNWs form a good electrical percolation network. As the Ag NWs were encapsulated with gold nanoshell, Biocompatibility of the newly

developed conductive rubber was improved by reducing much less Ag ion leaching than pure AgNW composite, while conductivity was also preserved as high as AgNW composite. In the our new stretchable conductor has novel percolated network due to the presence of the gold nanoshell on the surface of AgNW, which encouraged stable electrical properties under mechanical strain by localization of conducting materials during long drying process without additional surfactant that can degrade conductivity.

We also demonstrate a new class of the cardiac sock-mesh using soft gold shell nanowire rubber composite. The solution-processible thermoplastic composite enables molding and welding process to make large sized device with multi electrode arrays, resulted in integration with the large size of porcine heart. Our study shows simultaneous analysis through cardiac mapping and stereotactic pacing effect that offers location-irrelevant pacing, which can expend the potential application of stretchable electrode to biomedical devices especially for treatment various cardiac diseases.

4.2 Experimental Section

4.2.1 Synthesis of silver nanowires

Ultra-long silver nanowire was synthesized by polyol-mediated processes, modified from previous study to produce longer AgNWs[7]. 100ml of ethylene glycol (EG) was pre-heated at 175oC with 260rpm stirring. poly-

vinylpirrolidone (PVP, MW 360k, Sigma Aldrich) was dissolved in 30ml of EG and the solution was added after 20 minutes. After the temperature was saturated, 800μl of 4mM copper chloride (CuCl2·2H2O; Sigma Aldrich) solution was added. Silver nitrate (AgNO3, Strem Chemical Inc., USA) solution was prepared with 0.095M concentration in EG and the solution was injected with 180 ml/hr 10 minutes after copper solution was injected. After the injection was finished, stirring was stopped and the synthesis reaction was kept for 20 minutes. After the reaction was over, the AgNWs solution was diluted with water (1:4) and was centrifuged at 3000 RPM for 10 minutes. The washing process was repeated 3 times to remove PVP of AgNWs. The washed AgNW was redispesed in water to encapsulate with gold nanoshell.

4.2.2 Preparation of gold shell silver nanowire/SBS composite film

Gold shell silver nanowires (Au@Ag) were dispesed in toluene with 30mg/ml. the Au@Ag solution was mixed with SBS dissolved solution (1:10 in toluene) with appropriate concentration. Optimized concentration showing highest stretchability is 45 wt% of Au@Ag nanowire in the Au@Ag/SBS composite. The mixed solution was poured in glass mold and dried at room temperature, 55 ^{o}C and 85 ^{o}C hotplates. Each Film sample was prepared after roll press of two sheets under 150^{o}C.

4.2.3 Microscopic image

Microscopy images were taken by field emission scanning electron microscope (FE-SEM, JSM-6701F, JEOL, Japan) and High resolution transmission electron microscopy (HRTEM, JEM-2100f, JEOL, Japan) Focused Ion Beam SEM (FIB-SEM, AURIGA, Carl Zeiss, Germany) was performed for nano-sized cross-sectional image.

4.2.4 Electrical characteristics

Conductivity was measure by four-point probe method using keithley 2400. Thickeness of film was measured by scanning electron microscope (SEM, S-1000M, Hitach, Japan) Stretchability was determined at the strain while the 2 wire resistance was increased more than xx times over.

4.2.5 Mechanical characteristics

The film sample was prepared in mm (length) x mm (width). Strain-stress curve was measure with xx mm/min using Universal Testing Machine (UTM, Instron-5543, Instron, USA). For mechanical test of the cardiac mesh, the two unit meshes were welded. The welded site was centered and the mesh with welding line in the middle was divided into a 5-layer bottom part and 3-layer top part. The divided mesh was cut into mm(length) x 35mm(width) and tested with xx mm/min

4.2.6 Electrochemical characteristics

Impedance and cyclic voltammetry (CV) of electrode was measured (CHI660E, CH Instruments, Inc., USA) by 3-electrode system in 0.9% sodium chloride aqueous solution. All electrode potential was measured in reference to Ag/AgCl electrode and a large platinum electrode was used as a counter electrode. CV was performed between -0.6 V to 0.9 V vs Ag/AgCl with sweep rate of 0.1 V/s. Impedance measurement was performed from 0.1 Hz to 100,000 Hz under 0.5 V. Voltage transient measurement was performed with biphasic current pulse which was +/-2 mA current and 10ms pulse width.

4.2.7 Electrical deposition of PEDOT

0.01M of 3,4-Ethylenedioxythiophene (EDOT, 97% Alfa Aesar, USA) and 0.01M of Lithium perchlorate (LiClO4, Sigma Aldrich, USA) were dissolved in acetronitrile (Sigma Aldrich, USA). The fabricated mesh electrode was dip into the solution and galvanostatic electrodepostion was performed under 0.1 mA of current using 2-electrode system (potential vs. Ag/AgCl reference electrode) for 1000s.

4.3 Result and Discussion

4.3.1 Fabrication of biocompatible Ag@Au/SBS composite

Silver nanowire (AgNW) has been widely utilized as many flexible and stretchable electrodes, expanding to be even employed to bio-medical devices due to its high intrinsic electrical conductivity and good mechanical flexibility. However, one of big obstacle hindering the biomedical application of AgNW is the toxicity rising from leaching of Ag^{+} ions. In contrast, gold (Au) is known as biocompatible and resistance to oxidation but main limitation rises from its low intrinsic conductivity. We synthesized Ag@Au core shell nanowires by encapsulating AgNW with thick shell of Au, achieving excellent in both electrical conductivity and biocompatibility. However, it is very challenging, in general, to synthesize such structure without galvanic reaction between Ag and Au. The hollow Au/Ag alloy nanostructures resulted from the galvanic reaction may degrade electrical property and biocompatibility of Ag@Au core shell nanowires. Despite many attempt to synthesize Ag@Au core shell structure with suppression of galvanic replacement reaction, slow injection rate of $HACl_4$ solution hinder from large scale synthesis and until now, only thin layer of Au shell synthesis had been reported[8].

We successfully synthesized thick gold nanoshell on AgNW with completely inhibiting galvanic replacement reaction by using the sulfite

ligand (sodium aurothiosulfate, $Na_2Au(SO_3)_2$) (Figure 4.1a). Sulfite ligand plays very important role in epitaxial deposition of Au on to Ag surface. The sulfite ligand selectively binds to Au cations thereby lowering reduction potential with high stability but not to Ag surface which prevent any ligand-assisted oxidative etching. Since sulfite coordinated Au precursor exhibit high stability, slow injection of Au precursor is not necessarily thereby enabling large scale synthesis. Also, by controlling concentration of silver nanowires in the reaction, we could control the thickness of Au shell deposited on to Ag surface. The synthesized Ag@Au nanowires (NW) had an average overall diameter of 180nm with average Au shell thickness of 30nm. After the ligand of the synthesized Ag@AuNW was exchanged to hexylamine, the Ag@AuNW dispersed in toluene, thus, Ag@AuNW and SBS composite (Ag@AuNW/SBS) was fabricated by mixing with SBS solution (dissolved SBS in 10 times weight of toluene) (Figure 4.1b), achieving high conductive and biocompatible stretchable conductor. The SEM image shows Ag@Au nanowires, and the inset shows backscatter image demonstrating clear contrast between AgNW core and Au shell (Figure 4.1c). Energy-dispersive X-ray spectroscopy (EDS) mapping show signal of Ag, Au elements which further confirm the core shell structures of Ag@AuNW (Figure 4.1d). It is also noteworthy that galvanic replacement reaction is completely inhibited which etching or hollow structure formation is not observed. We also demonstrate the biocompatibility of Ag@AuNW

which is more desirable for clinical human use. AgNW, Ag@AuNW, Ag@AuNW/SBS composites were dispersed in Dulbecco's Modified Eagle's Medium (DMEM) solution for 3 days in cell incubator to mimic clinical environment and amount of Ag+ ion leached was analyzed by inductively coupled plasma mass spectroscopy (ICP-MS) (Figure 4.1e). As a result, Au shell could effectively prevent Ag ions from leaching (5.8% compare to pristine AgNW) and blending with SBS further blocked Ag+ ion leaching down to 1.2%. The toxicity of Ag@Au were further confirmed by live dead assay with H9C2 cell lines (Figure 4.1f). It demonstrated better biocompatibility in Ag@AuNW than bare AgNW, and biocompatibility further enhanced after incorporating SBS to Ag@AuNW which in agreement with ICP-MS data.

The biocompatible Ag@Au/SBS composite exhibited high stretchabiltiy with stable electrical performance. Localization of the conductive filler can improve stretchability by effective percolation network[9,10]. During the drying process of the Ag@AuNW/SBS solution, the Ag@AuNW showed clustering effect which densified the electron pathway even under mechanical deformation. The mixture of Ag@AuNW and SBS in toluene with an appropriated concentration was poured on the glass mold. Drying at low temperature (room temperature; 20 ^{o}C) maximized the clustering effect by lengthening the drying time over two days. The SEM image shows clustering island mostly composed of Ag@AuNW (Figure 4.2a and 4.2b).

While stretching, most strain was applied between clustering regions that is mainly comped with SBS, forming SBS bridges (Figure 4.2b). However, the ultra-long Ag@AuNW still maintained electrical percolation structure on the SBS bridges, improving stable conduction while stretching. On the other hand, Ag@Au NW/SBS showed homogeneously distribution of Ag@AuNW when dried under 55^{o}C and 85^{o}C, and did not show clustering island and SBS bridges. As a result, Ag@AuNW reinforced the rubber composite, showing stiff strain-stress curve, whereas, SBS bridge structure, covered reinforced stiff island region by absorbing applied strain, resulting in low modulus of Ag@AuNW/SBS composite (Figure 4.3a). Figure 4.3b shows the stretchability and conductivity of the Ag@AuNW/SBS composite depending on the filler concentration. The conductivity showed escalating tendency in correspondence of increase in contents of the Ag@AuNW, showing up to 35,000 S/cm as its maximum conductivity with at 70 wt% of Ag@Au NW which is the highest amongst previously reported free-standing composites. Meanwhile, 45% of Ag@Au/SBS composite showed highest stretchability (180%), implying threshold contents of the SBS required to form the SBS bridges with conductivity still showing high 19,783S/cm. The conductivity of the Ag@AuNW/SBS composite while stretching was measured depending on different the drying temperature condition. With 20oC drying process, the densified Ag@AuNW clustering region and percolated conductive network on the SBS bridge led to stable performance

of the conductivity under stretching up to 180 % (Figure 4.3c).

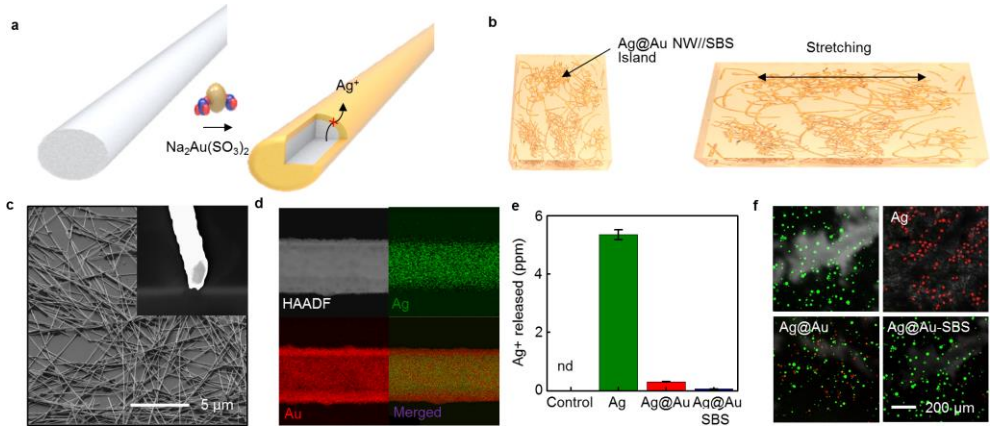

Figure 4.1 Biocompatible gold shell silver nanowire (Ag@Au NW) and SBS nanocomposite.

(a) Synthesis of gold shell on the silver nanowire without garvanic reaction. (b) Stretchable conductor composed of Ag@AuNW and SBS rubber composite. (c) The SEM image of Ag@AuNW. (d) EDS mapping to confirm the core shell structure of Ag@AuNW. (e) Inductively coupled plasma mass spectroscopy (ICP-MS) data to analyze Ag ion leaching from control and bare AgNW, Ag@AuNW, and Ag@AuNW/SBS composite. Control data was achieved from SBS rubber. (f) Live dead assay to confirm cell toxicity of the bare AgNW, Ag@AuNW, and Ag@AuNW/SBS.

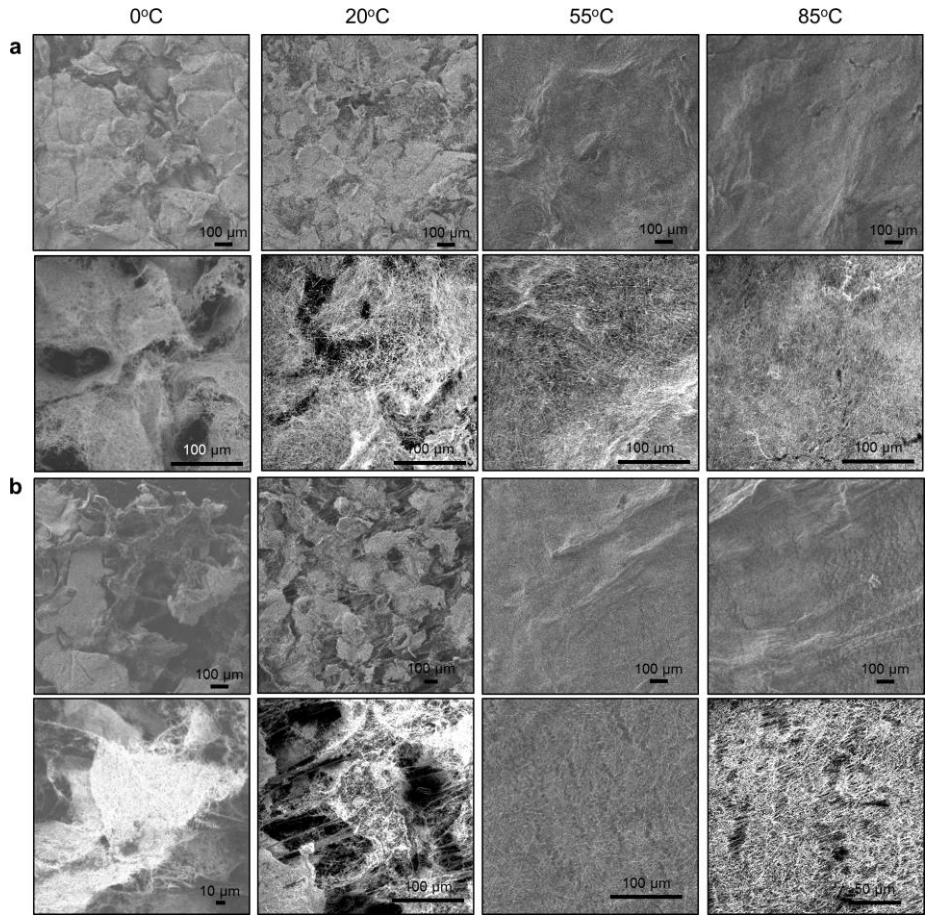

Figure 4.2 SEM images of Ag@Au/SBS composites depending on the fabrication temperature.

(a) Ag@Au NW/SBS composited depending on the fabrication processing temperature and (b) its stretching under 30% strain.

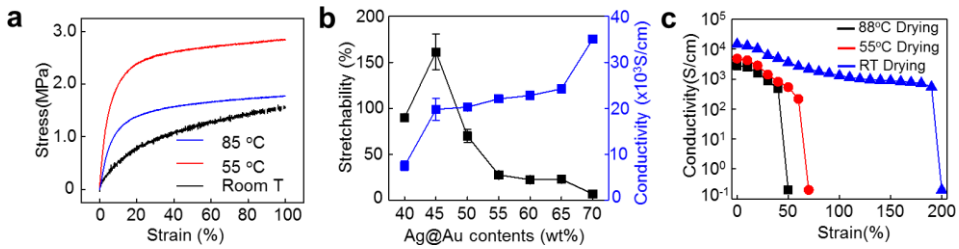

Figure 4.3 Mechanical and electrical performance of the Ag@Au/SBS composite.

(a) The strain-stress curve of Ag@AuNW/SBS depending on the fabrication processing temperature. (b) Measurement of stretchability and conductivity depending on the the Ag@AuNW contents in stretchable conductor. (c) Conductivity change under mechanical stretching of the Ag@AuNW/SBS

4.3.2 Improvement of electrochemical performance for bio-medical electrode

In order to exploit the Au@Ag/SBS composite as a epicardial electrode, we modified surface of electrodes to lower impedance and increase charge injection through electropolymerization of 3,4-Ethylenedioxythiophene (EDOT) on the electrodes (Figure 4.4a). First, Au@AgNW/SBS composite and SBS was patterned in serpentine shaped mold and the Au@AgNW/SBS was sandwiched by SBS layer without covering electrode areas. Then this fabricated electrode line was encapsulated with Ecoplex for insulation purpose. The impedance of epicardial electrodes reduced after electrodeposition of Poly(3,4-ethylenedioxythiophene) (PEDOT) (Figure 4.4b). When the epicardial electrode was stretched up to 30%, the electrochemical property was maintained. In cyclic voltammogram, cathodal charge storage capacity was increased from12.98 mC/cm^2 to 80.11mC/cm^2 after surface modification and the CV curve was maintained when it was stretched up to 30% strain (Figure 4.4c). Figure 4.4d shows that the same amount of charge injection occurred with applied less potential at the PEDOT coated epicardial electrodes under condition of 2mA biphasic current during 2ms. High electrohemical properties of the electrode as well as its high conductivity of the intrinsic materials improved the recording signal from the rat's heart[10]. Figure 4.4e shows intracardial signal from the epicardial surface from a pair of single electrode and Figure 4.4f shows that

the heart rate was accelerated by pacing rate when the electrical stimulation was applied with 260ms of cycle length.

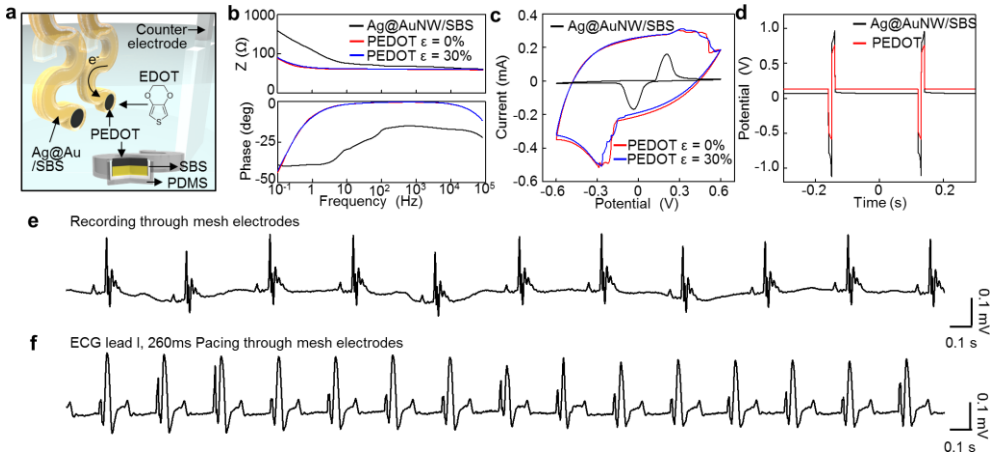

Figure 4.4 Electrochmical properties of Ag@Au/SBS electrode.

(a) An illustration of the electrodeposition of PEDOT on the Ag@AuNW/SBS electrode. (b) Measurement of impedance and phase of Ag@AuNW/SBS electrode before and after PEDOT deposition and stretched Ag@AuNW/SBS electrode with PEDOT. (c) Cyclic voltammetry of Ag@AuNW/SBS electrode before and after PEDOT deposition and stretched Ag@AuNW/SBS electrode with PEDOT. (d) Charge injection under 2mA biphasic current stimulation on the Ag@AuNW/SBS electrode before and after PEDOT deposition. (e) Recorded intracardiac electrogram from PEDOT coated Ag@AuNW/SBS electrode at rat heart. (e) Surface ECG (lead l) of rat while pacing (260 cycle length) with PEDOT coated Ag@AuNW/SBS electrode.

4.3.3 Customized 3D cardia mesh on porcine heart

To integrate the electrode with the large size of porcine heart, arrays of the electrodes are required to wrap the heart around. Figure 4.5a describes fabrication step for multi-polar cardiac mesh and its layered formation. Rounded heart shape was simplified to design electrode mesh arrays. The simplified model was spreaded to a shape of a fan composed of series of unit meshes. SBS meshes and Au@AgNW/SBS electrodes was layered to prepare a single unit mesh through welding process, consisting of six pairs of electrodes. Due to the thermoplastic property of SBS rubber, the SBS mesh and SBS in the Au@AgNW/SBS composite could be diffused and welded each other under heat and pressure.[12] After then, the single unit meshes were arrayed and welded each other to make final multi-polar cardiac mesh sock. To firmly encapsulate side of conducting layer, silicon rubber (Ecoplex, USA) was coated except opened electrodes zone. Figure 4.5b shows that a photograph of the multi-polar cardiac mesh. Prepared cardiac mesh could be customized based on the MRI cardiac image (Figure 4.5c). The block copolymer structure of SBS rubber has shape memory effect as the polymer has soft segment for switching and hard segment for the cross-links.[13] After welding both ends of the cardiac mesh, we wrapped it in a 3D printed heart to fit the size. 3D printed heart kept the shape of mesh with heart shape during heating and cooling process (Figure 4.5d). Although the cardiac mesh was stretched to fit the origin size of heart, the

resistance of the electrode almost did not change after customizing process (Figure 4.5e). Each resistance of electrode line were measured under 30% strain which is from the circumferential strain during the systole and diastole cycle (Figure 4.5f) and the resistance change of the middle sized electrode lines were measured during cyclic strain test (Figure 4.5g). Stale electrical performance under mechanical strain and cyclic strain enable to impart the cardiac mesh to measure the cardiac signals and stimulate the heart despite of cyclic pumping activity. We also measure the modulus of the cardiac mesh by dividing into regions and directions (Figure 4.5h) to confirm that the cardiac mesh would not impede the cardiac pumping activity. Since the modulus of the meshes were much lower than the modulus of porcine myocardium which data was referred from ref[14], it was expected that cardiac mesh would not inhibit the pumping activity confirmed by previous study based on various simulations and experiments that soft, low modulus mesh does not impede on the movement of ventricles and left ventricle (LV) pressure.[15]

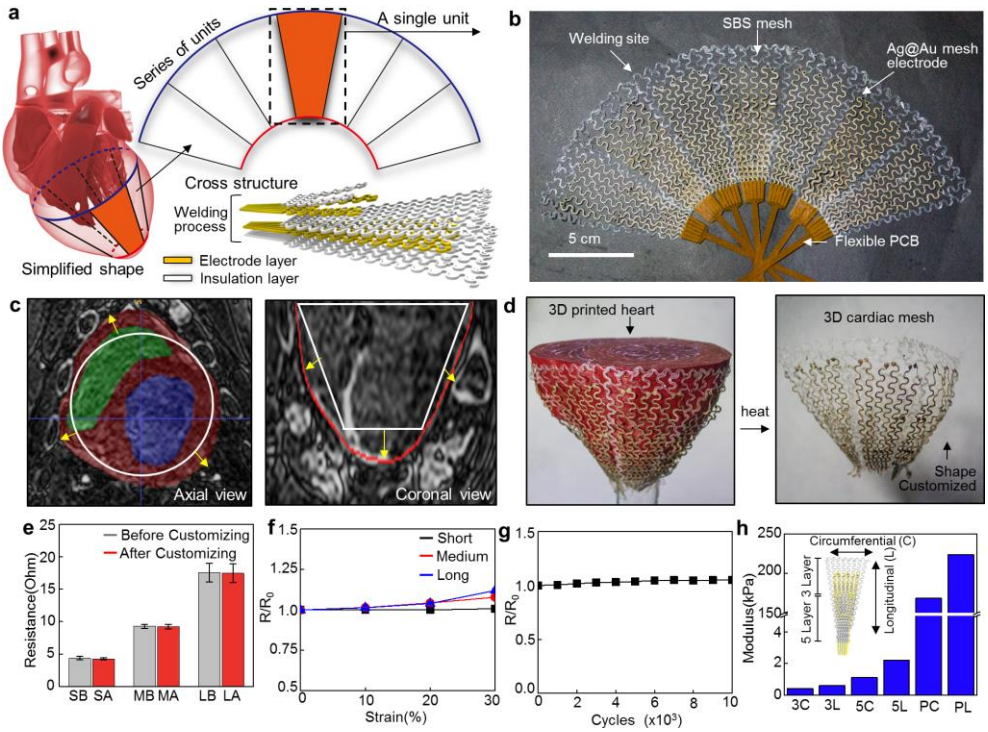

Figure 4.5 Fabrication of 3D cardiac sock-mesh and electrical and mechanical properties.

(a) A demonstration of cardiac mesh design derived from real heart shape. (b) Unfolded multipolar mesh connected to FPCB. (c) Axial and coronal MRI views of live porcine heart. (d) Customizing of multipolar cardiac mesh. Multipolar cardiac mesh covering 3D printed heart (left). After the customizing process, the mesh structure is fixed as the shape of the 3D printed heart (right). (e) Unchanged resistances of mesh electrode lines. (SB,SA : short electrodes; MB,MA : Middle electrodes; LB,LA : Long electrodes). (f) Changes in the resistance under strain. (g) Cyclic test of mesh electrode line; strain=30%. (h) Modulus of mesh depending on the

layer section of the mesh and comparision with modulus of porcine heart depending on the heart direction (PC: Porcine circumferential direction; PL: Porcine longitudinal direction).

4.3.4 Recoding of cardiac activity and streotactic pacing

We tested the 3D cardiac mesh on the porcine heart to measure consistently intrinsic myocardial electrical activities and to investigate electrical stimulation through 3D cardiac mesh in vivo (Figure 4.6a). Before the cardiac mesh was implanted in position, Left anterior descending coronary artery (LAD) was occluded with balloon catheter to induce acute myocardial infarction. Figure 4.6b shows a photograph of the 3D cardiac mesh implanted on the swine heart. Intracardiac electrogram in Figure 4.6c were measured simultaneously at each position following one hour LAD occlusion. Due to the LAD occlusion, wide QRS duration informed that myocardial tissues were damaged at left ventricles anterior (LVa) compared to normal position. Especially at the position of number 3 to 5 which showed delayed conduction and ST elevation that obviously resulted from myocardial injuries. Figure 4.6d shows the time-dependent comparison of the heart signal from the damaged tissue portion due to LAD occlusion and the normal tissue portion. As myocardial infarction became more severe, cardiac function worsened, eventually leading to ventricular tachycardia (VT) which means faster heartbeat than normal and ventricular fibrillation (VF) which means disordered heartbeat. When VT was started, the signal from the normal tissue showed regular and fast heartbeat, but the signals from damaged tissue already showed disordered pattern. Figure 4.7a showed pairs of electrode position on the reconstructed image from MRI images.

Local electrical activity was recorded from 24 pairs of electrodes on the epicardium (Figure 4.8) and an activation map was constructed by recorded bipolar intracardial electrogram (Figure 4.7b) which showed the time difference of the maximum slope of the voltage based on the surface ECG (lead ll) after interpolation. From the isochronal cardiac activation mapping, the damaged heart muscle could be detected and it corresponded to voltage map which is the map of difference of highest and lowest voltage (Figure 4.7c).

We further estimated effects of the electrical stimulation depending on the sites of pacing. Average contractility (dP/dtmax) was calculated under 3D coordinated electrical stimulation based on the pressure curve while pacing is simultaneously occurred. Figure 4.7d shows that pacing along the lateral side of the LV are relatively effective to restore cardiac function. A single pressure curves are representative high, medium, and low slope of pressure (Figure 4.7e). This sterotactical pacing by 3D cardiac mesh could expand new potential of cardiac synchronization therapy for patients who were ineffective by conventional cardiac pacing catheter method.

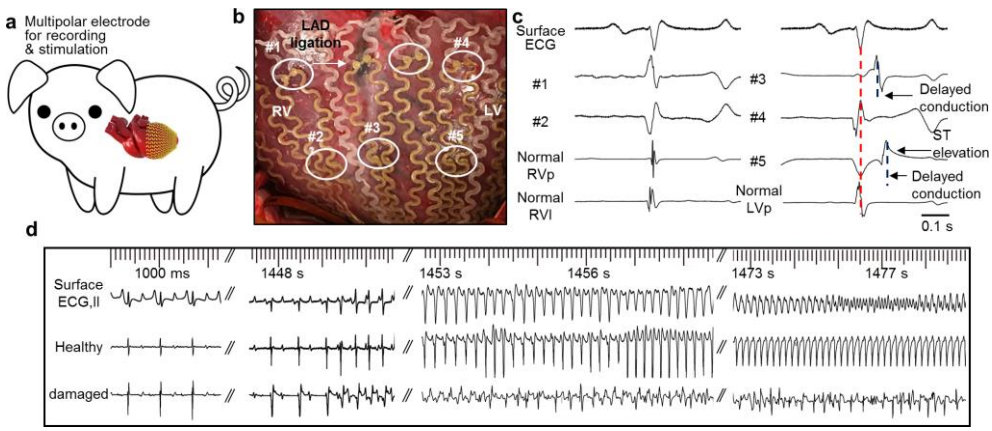

Figure 4.6 Recording intracardia electrogram form 3D cardiac sock-mesh *in vivo.*

(a) An illustration of implantation of 3D cardiac mesh on swine heart in vivo. (b) A photograph of implanted 3D cardiac mesh on LAD occulated heart. (c) Intracardiac electrogram from 3D cardiac mesh one hour after LAD occlusion. Each electrogram strip corresponds to the electrodes in (b). (d) Surface ECG and intracardiac electrogram form healthy tissue and damaged tissue over time. It proceeded in the order of Sinus rhythm, VT initiation, VT, and VF according to time.

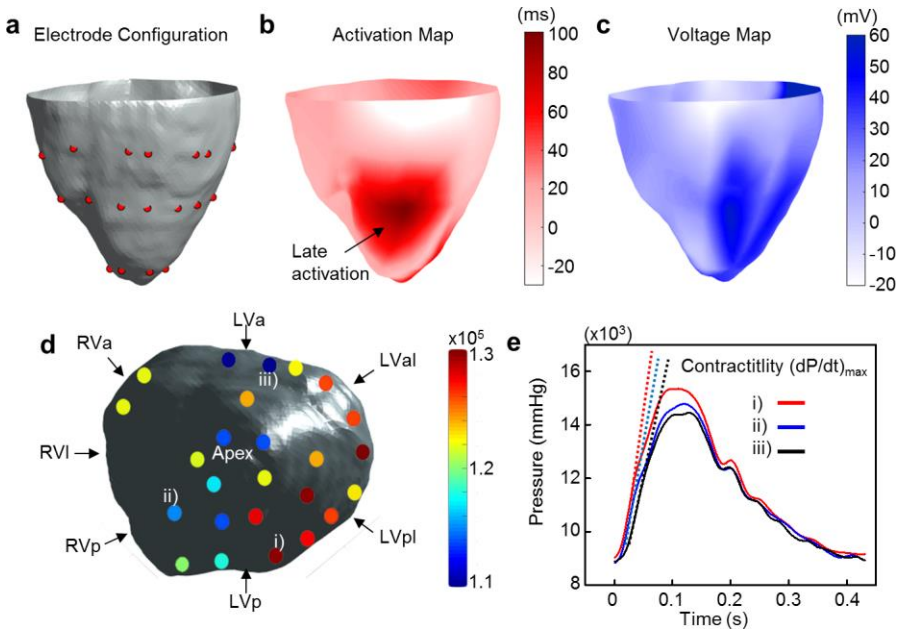

Figure 4.7 Mapping based on simultaneouly recorded signals and hemodynamic response from streotactic pacing.

(a) Bipolar electrode configuration on the 3D reconstructured image from MRI. (b) Interpolation of the activation time and its map on the 3D recon model. (c) Interpolation of voltage map and tis map on the 3D model. (d) Contractility (dP/dtmax) was shown under 3D coordinated electrical stimulation. (e) A single pressure curve show high, middle low contractility by stereotactic pacing.

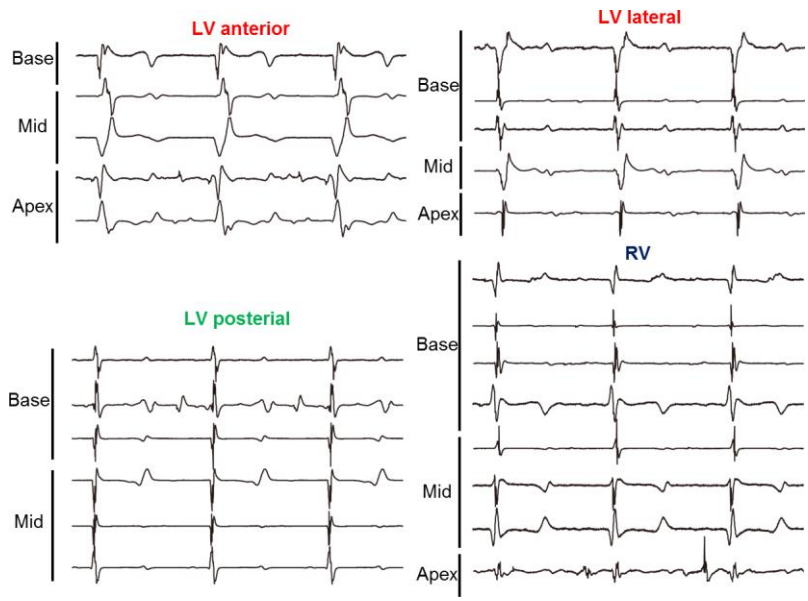

Figure 4.8 Recorded intracardiac electrograms from multi-polar 3D cardiac mesh-sock electrodes after one hour LAD ligation.

4.4 Conclusion

Recent research into stretchable electrodes has led to many breakthroughs in application to from wearable electronics to biomedical implantable devices. Here, we successfully encapped Ag NW with gold nano shell to prevent Ag ion leaching out, achieving biocompatible metal nanowire. With blending the Ag@AuNW and SBS rubber, stretchable Ag@Au core shell nanowire SBS rubber composite was achieved as highly conductive and biocompatible stretchable conductor. This outstanding performance of stretchable conductor can be fabricated in a soft multi-polar 3D cardiac mesh that can be exploited as a cardiac monitoring electrode and pacing electrode with disease-specific simulation without limitation of electrode position on the epicardium.

4.5 Reference

(1) Cantwell, C. D.; Roney, C. H.; Ng, F. S.; Siggers, J. H.; Sherwin, S. J.; Peters, N. S. *Comput. Biol. Med.* **2015**, *65*, 229.

(2) Harrison, L.; Ideker, R. E.; Smith, W. M.; Klein, G. J.; Kasell, J.; Wallace, A. G.; Gallagher, J. J. *Pacing Clin. Electrophysiol.* **1980**, *3*, 531.

(3) Worley, S. J.; Ideker, R. E.; Mastrototaro, J.; Smith, W. M.; Vidaillet, H.; Chen, P. S.; Lowe, J. E. *Pacing Clin. Electrophysiol.* **1987**, *10*, 21.

(4) Xu, L.; Gutbrod, S. R.; Bonifas, A. P.; Su, Y.; Sulkin, M. S.; Lu, N.; Chung, H. J.; Jang, K. I.; Liu, Z.; Ying, M.; Lu, C.; Webb, R. C.; Kim, J. S.; Laughner, J. I.; Cheng, H.; Liu, Y.; Ameen, A.; Jeong, J. W.; Kim, G. T.; Huang, Y.; Efimov, I. R.; Rogers, J. A. *Nat. Commun.* **2014**, *5*, 3329.

(5) Dvir, T.; Timko, B. P.; Brigham, M. D.; Naik, S. R.; Karajanagi, S. S.; Levy, O.; Jin, H.; Parker, K. K.; Langer, R.; Kohane, D. S. *Nat. Nanotechnol.* **2011**, *6*, 720.

(6) Gong, S.; Schwalb, W.; Wang, Y.; Chen, Y.; Tang, Y.; Si, J.; Shirinzadeh, B.; Cheng, W. *Nat. Commun.* **2014**, *5*, 3132.

(7) Jose Andres, L.; Fe Menendez, M.; Gomez, D.; Luisa Martinez, A.; Bristow, N.; Paul Kettle, J.; Menendez, A.; Ruiz, B. *Nanotechnology* **2015**, *26*, 265201.

(8) Yang, Y.; Liu, J.; Fu, Z. W.; Qin, D. *J. Am. Chem. Soc.* **2014**, *136*, 8153.

(9) Matsuhisa, N.; Kaltenbrunner, M.; Yokota, T.; Jinno, H.; Kuribara, K.; Sekitani, T.; Someya, T. *Nat Commun* **2015**, *6*, 7461.

(10) Wang, Y.; Zhu, C.; Pfattner, R.; Yan, H.; Jin, L.; Chen, S.; Molina-lopez, F.; Lissel, F.; Liu, J.; Rabiah, N. I.; Chen, Z.; Chung, J. W.; Linder, C.; Toney, M. F.; Murmann, B.; Bao, Z. *Sci. Adv.* **2017**, *3*, e1602076.

(11) Ripart, A.; Mugica, J. *Pacing Clin. Electrophysiol.* **1983**, *6*, 410.

(12) Choi, S.; Park, J.; Hyun, W.; Kim, J.; Kim, J.; Lee, Y. B.; Song, C.; Hwang, H. J.; Kim, J. H.; Hyeon, T.; Kim, D. H. *ACS Nano* **2015**, *9*, 6626.

(13) Lendlein, A.; Kelch, S. *Angew. Chem., Int. Ed.* **2002**, *41*, 2034.

(14) Pham, T.; Sun, W. *J. Mech. Behav. Biomed. Mater.* **2012**, *6*, 21.

(15) Park, J.; Choi, S.; Janardhan, A. H.; Lee, S. Y.; Raut, S.; Soares, J.; Shin, K.; Yang, S. X.; Lee, C.; Kang, K. W.; Cho, H. R.; Kim, S. J.; Seo, P.; Hyun, W.; Jung, S.; Lee, H. J.; Lee, N.; Choi, S. H.; Sacks, M.; Lu, N. S.; Josephson, M. E.; Hyeon, T.; Kim, D. H.; Hwang, H. J. *Sci. Transl. Med.* **2016**, *8*.

Bibliography

1. Publications

(1)J. Park*, **S. Choi***, A. H. Janardhan, S.-Y Lee, S. Raut, J. Soares, K. Shin, S. Yang, C. Lee, K.-W. Kang, H. R. Cho, S. J. Kim, P. Seo, W. Hyun, Su. Jung, H.-J. Lee, N. Lee, S. H. Choi, M. Sacks, N. Lu, M. E. Josephson, T. Hyeon, D.-H. Kim, and H. J. Hwang, "Electromechanical cardioplasty using a wrapped elasto-conductive epicardial mesh," ***Sci. Transl. Med.*** 8, 344ra86 (2016) ***equal contribution**.

(2) **S. Choi**, H. Lee, R. Ghaffari, T. Hyeon, D.-H Kim, Recent Advances in Flexible and Stretchable Bio-Electronic Devices Integrated with Nanomaterials, ***Adv. Mater.*** 28, 4203, (2016)

(3) **S. Choi**, J. Park, W. Hyun, J. Kim, J. Kim, Y. B. Lee, C. Song, H. J. Hwang, J. H. Kim, T. Hyeon, D.-H. Kim, "Stretchable Heater Using Ligand-Exchanged Silver Nanowire Nanocomposite for Wearable Articular Thermotherapy," ***ACS Nano.*** 9, 6626 (2015)

(4) S. Lim, D. Son, J. Kim, Y. B. Lee, J.-K. Song, **S. Choi**, D. J. Lee, J. H. Kim, M. Lee, T. Hyeon, D.-H. Kim,"Transparent and Stretchable Interactive Human Machine Interface Based on Patterned Graphene Heterostructures," ***Adv. Funct. Mater.*** 25, 375 (2015).

(5)S. Jung, J. H. Kim, J. Kim, **S. Choi**, J. Lee, I. Park, T. Hyeon, D.-H. Kim, "Reverse-Micelle- Induced Porous Pressure-Sensitive Rubber for Wearable Human-Machine Interfaces," ***Adv. Mater.*** 26, 4825 (2014).

2. Patents

(1) **S. Choi**, T. Hyeon, D.-H. Kim, S.-J. Ryoo, J. Park, W. Hyun, "Flexible heating system and manufacturing method thereof," Korea Patent, (10-1641314), 2016.07.14

(2) D.-H. Kim, T. Hyeon, J. Park, **S. Choi**, "Elastomeric Heating Element Comprising Silver Nanowire," PCT Patent, (PCT/KR2015/003208), 2015.04.14

(3) D.-H. Kim, T. Hyeon, J. Park, **S. Choi**, "Surface-Modified Silver Nanowire and Process for Preparing the Same," PCT Patent, (PCT/KR2015/003207), 2015.03.31

(4) D.-H. Kim, T. Hyeon, J. Park, **S. Choi**, "Electrically conductive composite materal," Korea Patent, (10-2015-0038616), 2015.03.20

(5) D.-H. Kim, T. Hyeon, H. J. Hwang, J. Park, **S. Choi**, "Mesh Electrode for Global Resynchronization Therapy and Process for Manufacturing the Same," PCT Patent, (10-2014-0156309),

2014.11.11

(6) D.-H. Kim, T. Hyeon, H. J. Hwang, J. Park, **S. Choi**, "Mesh Electrode for Global Resynchronization Therapy and Process for Manufacturing the Same," Korea Patent, (10-2014-0156309), 2014.11.11

(7) D.-H. Kim, T. Hyeon, J. Park, **S. Choi**, "Surface-Modified Silver Nanowire and Process for Preparing the Same," Korea Patent, (10-2014-0052995), 2014.04.30

3. Conference presentation

(1) **S. Choi**, H. J. Hwang, and D.-H. Kim, "Electromechanical CardioplastyUsing a Highly Conductive and Elastic Epicardial Mesh" International Conference on Electronic Materials and Nanotechnology for Green Environment, Jeju, Korea, Nov 9 (2016)

(2) **S. Choi**, and D.-H. Kim, "Soft, elastic, and conductive epicardial mesh for an electromechanical hug the heart" *2016 Korean Society of Industrial and Engineering Chemistry Fall Meeting, Korea*, Oct 28 (2016)

(3) **S. Choi**, J. Park, H. J. Hwang, T. Hyeon, and D.-H. Kim, "Elasto-

conductive epicardialmesh for electromehanicalcardioplasty*" 20th International Vacuum Congress, Busan, Korea*, Aug 24 (2016)

(4) **S. Choi**, and D.-H. Kim, "Soft and stretchable heater for wearable articular heat therapy using Ligand-Exchanged Silver Nanowire Nanocomposite" *2016 Material Research Society Spring Meeting, Pheonix, AZ, USA*, Mar 30 (2016)

(5) **S. Choi**, and D.-H. Kim, "Stretchable and Wearable Heater with Ligand-Exchanged Silver Nanowire Nanocomposite for Articular Thermotherapy" *2015 Korean Society of Industrial and Engineering Chemistry Fall Meeting, Jeju, Korea*, Nov 06 (2015)

Abstract

고전도성과 고신축성의 늘어나는 전도체는 스트레쳐블 디바이스와 웨어러블 디바이스의 발전에 중요한 역할을 한다. 고신축성 늘어나는 전도체의 전도성 충전제는 전기적 퍼콜레이션을 형성하여 성능을 결정하는데에 중요한 요소이다. 대표적인 충전제로, 그래핀, 탄소나노섬유 등의 탄소소재와 전도성 고분자가 쓰이며, 본래 전도도가 높은 특성을 띄는 금속성 나노소재를 이용한 신축성 전도체도 활발하게 연구 되고있다. 물질의 고유한 전도성 뿐만 아니라, 물질의 구조도 전도성과 신축성을 결정하는데 큰 영향을 미친다. 특히 1D 구조의 나노 물질은 높은 종횡비로 인해 전기적 퍼콜레이션을 형성하는데 유리하여 외력에 의한 변형에도 안정적인 전기적 성질을 보이는 신축성 전도체를 만들기 용이하다. 순수한 재료의 특성뿐만 아니라, 외력에 의해 전도체 자체에 스트레인을 최소화 시키는 구조적인 형태를 이용하여도 훨씬 더 안정적으로 구동되는 스트레쳐블 디바이스에 활용될 수 있으며, 이를 이용하여, 스트레인 센서를 이용한 웨어러블 디바이스와 늘어나는 전기소자의 전극, 에너지 디바이스 등으로 활용될 수 있다.

첫번째로 전도성이 높은 은나노와이어와 poly(styrene-butadien-styrene) (SBS) 엘라스토머를 이용하여 전도성 고무를 만들고 줄히팅 방식을 이용하여 늘어나는 전기히터를 제작하였으며, 이를 이용하여 관절의 온열치료에 적용할 수 있는 온열치료기를 개발하였다. 친수성의 은

나노와이어의 리간드 교환반응을 이용하여 톨루엔에 분산된 SBS고무에 균일하게 섞이도록 만들어 높은 전도성을 띄는 전도성 고무를 만들고 이를 설펜틴 구조로 제작하여 늘어나도 저항이 안정적으로 유지되어 구부러지는 관절에도 효과적으로 열을 전달 할 수 있었다. 컴퓨터 칩이 장착된 밴드와 결합하여 휴대성을 높인 온열치료기를 제작하였으며, 컴퓨터 시뮬레이션과, 생리학적인 면에서의 효과도 검증하였다.

두번째로 리간드 교환 반응을 거친 은나노와이어와 SBS고무 복합체와 SBS고무를 이용하여 심외막 그물망를 만들어 심장에 감싸, 기계적 심장성형과 더불어 심장의 전기적 특성을 향상시키는 체내삽입형 메디칼 디바이스를 제작하였다. 설펜틴 패터닝을 통하여 기계적 특성이 심장조직과 비슷하게 만든 유연한 심외막 그물망이 심장을 밀접하게 감싸 심실벽의 스트레스를 줄여, 심장의 부하를 덜어주는 역할도 할 수 있음을 확인하였다. 또한, 그것의 대면적 전극을 통해 전기적 자극을 가하여 심근경색 쥐 심장의 수축기능을 향상시킴을 확인함으로써, 실제 질병모델의 쥐에서 심장의 이완기에는 방해를 주지 않지만, 수축 시 기능을 기계적, 전기적 접근방법의 치료를 가능하게 하였다.

마지막으로, 생체 적합한 스트레처블 바이오메디칼 디바이스를 위해 새로운 생체적합성, 신축성 전도체가 이식 가능한 생체 의학 장치로 널리 적용됨에 따라 생체 적합성이 향상되는 것이 주요 문제 중 하나이다. 전도성 나노컴퍼짓을 개발하였다. 은나노와이어 표면을 생체 적합한 금으로 코팅하여 생체에 적합한 Ag@Au 코어쉘 와이어를 개발하였다. 은

나노와이어 표면의 금의 상호작용으로 인하여, 늘어나는 전도체에 효과적인 퍼콜레이션을 이루어 기존에 개발된 전도성 고무보다 더욱 신축성이 뛰어나면서 고전도성을 띄는 생체친화적 고무복합체를 개발하였다. 이를 이용하여, 3D모양의 다극성 심장그물망을 제작하였으며 심장 전면에 걸친 신호를 더욱 세부적인 위치에서 레코딩 하여 병변부위를 확인할 수 있게 하였고, 그에 따른 위치별 전기적 자극을 가능하게 하였다